

Air-sea interaction processes during hurricane Sandy: Coupled WRF-FVCOM model simulations

Siqi Li^{*}, Changsheng Chen

School for Marine Science and Technology, University of Massachusetts-Dartmouth, New Bedford, MA 02744, United States



ABSTRACT

A fully-coupled atmospheric-ocean model was developed by coupling WRF (Weather Research and Forecasting Model) with FVCOM (the unstructured-grid, Finite-Volume Community Ocean Model) through the Earth System Model Framework (ESMF). The coupled WRF-FVCOM is configured with either hydrostatic or non-hydrostatic oceanic dynamics and can run with wave-current interactions. We applied this model to simulate the 2012 Hurricane Sandy in the western Atlantic Ocean. The experiments examined the impact of air-sea interactions on Sandy's intensity/path and oceanic responses under hydrostatic and non-hydrostatic conditions. The results showed that the increased storm wind rapidly deepened the mixed layer depth when ocean processes were included. Intense vertical mixing brought cold water in the deep ocean towards the surface, producing a cold wake within the maximum wind zone underneath the storm. This process led to a sizeable latent heat loss from the ocean within the storm, and hence rapid air temperature and vapor mixing ratio drop above the sea surface. The storm intensified as the central sea-level pressure dropped. Improving air pressure simulation with ocean processes tended to reduce the storm size and strengthen its intensity, providing a better simulation of hurricane path and landfall. Turning on the non-hydrostatic process slightly improved the hurricane central sea-level pressure simulation and intensified the winds on the right side of the hurricane center. Hydrostatic and non-hydrostatic coupled WRF-FVCOMs captured Sandy-induced rapidly-varying flow over the shelf and the wind-induced surge level at the coast. The coupled models predicted a higher water elevation around the coastal areas where Sandy made landfall than the uncoupled model. The uncoupled and coupled models both showed more significant oceanic responses on the right side of the hurricane center, with a maximum during the Sandy crossing period when the clockwise-rotating frequency of Sandy wind was close to the local inertial frequency. The area with a maximum response varied with Sandy's translation speed, more prominent in the deep region than over the slope, and more substantial under the non-hydrostatic condition. The simulated ocean responses agreed with the theoretical work of Price (1981). The nonhydrostatic experiments suggest that to resolve a fully storm-induced convection process, the oceanic model grid configuration should meet the $O(1)$ criterion for the ratio of local water depth to the model horizontal resolution.

1. Introduction

The U.S. northeast coast is highly susceptible to extratropical and tropical cyclones (Bernier and Thompson, 2006; Chen et al., 2021a). Tropical cyclones can cause storm surges, torrential rainfall, coastal flooding, and severe damage to infrastructure, residential houses, trees, and in some cases, injury or death. Hurricane Sandy, which struck the eastern coast of the United States in October 2012, was one of the superstorms in history and caused severe disasters for the coastal region. It first appeared as a low-pressure cyclone and quickly strengthened into Tropical Storm Sandy over the Caribbean Sea on 22 October. It then upgraded to a hurricane after moving northward and crossing Jamaica and Cuba on 26 October. Sandy turned into an extratropical cyclone as cold air came into the center at around 21:00 (all the times are Coordinated Universal Time) on 29 Oct. and made landfall near Brigantine, New Jersey, at 23:30 (Blake et al., 2013). This hurricane produced strong winds (with maximum sustained winds of ~ 36 m/s observed in Atlantic City). The OceanSat-2 satellite images revealed that this

hurricane was characterized by a robust asymmetric wind field, with its maximum on its center's left and rear areas (Fig. 1) (<https://www.jpl.nasa.gov/images/pia16219-oscat-eyes-hurricane-sandy>). The storm winds produced high water and surge levels of ~ 4.4 and ~ 3.0 m and significant wave height of ~ 10 m, causing severe coastal inundation over New Jersey, New York City, and Long Island. 233 people died, and property damages were estimated to be \$71.4 billion (Diakakis et al., 2015).

Intensive studies have been conducted to discover the dynamics of hurricane formation (Charney and Eliassen, 1964; Anthes, 1974; Emanuel, 2003). The Sea Surface Temperature (SST) is an essential factor in the air-sea interaction of tropical cyclone (TC) dynamics. The TCs are fueled by the ocean mainly via latent and sensible heat fluxes, which are affected by SST (Schade and Emanuel, 1999). Since the marine bottom boundary parameterization for an atmospheric model is connected to the ocean through SST, high-accurate SST could improve the prediction of hurricane track and intensity by numerical meteorological models (Dare and McBride, 2011; Glenn et al., 2016; Mooney et al., 2016; Li

* Corresponding author.

E-mail address: sli4@umassd.edu (S. Li).

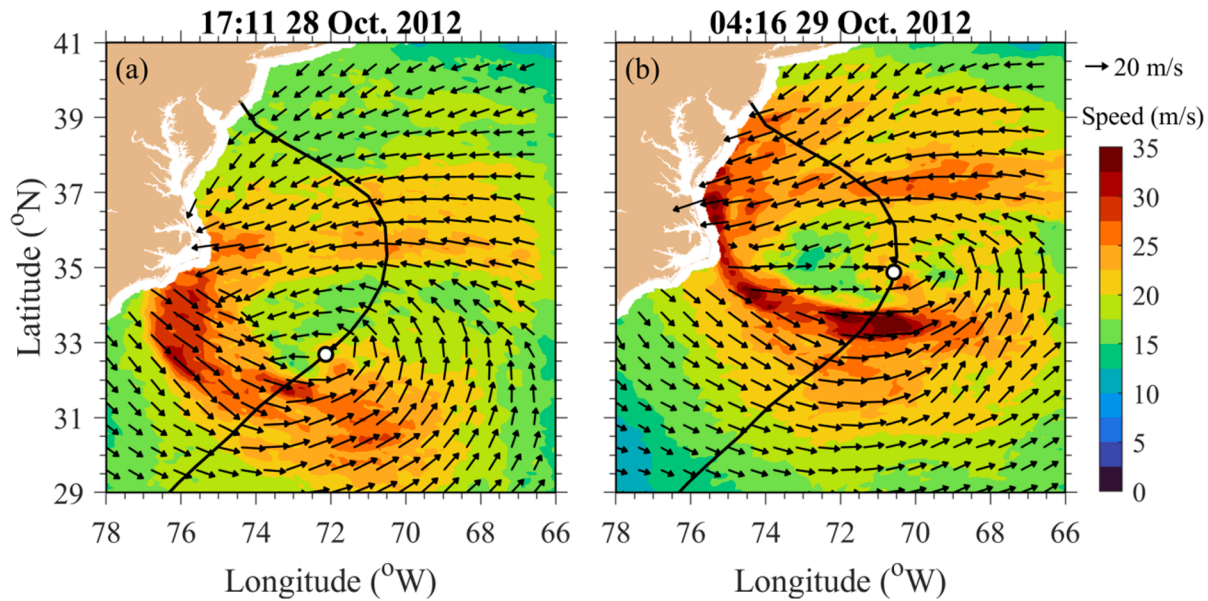


Fig. 1. Oceansat-2 satellite images of Hurricane Sandy wind vectors at the 10-m height at 17:11 on 28 Oct. (a) and 04:16 on 29 Oct. (b), 2012. The resolution was \sim 12 km. The data were downloaded at <https://cmr.earthdata.nasa.gov>. Black arrows: wind vectors at the 10-m height; color images: the 10-m wind speed; black lines: the observed trajectory of the hurricane center; white points: the hurricane center locations.

et al., 2020).

Three approaches were taken to improve the marine boundary layer parameterization, including 1) adding either satellite-derived or ocean model-produced SSTs as a boundary condition at the sea surface (Cione and Uhlhorn, 2003; Zeng and Beljaars, 2005); 2) implementing an ocean mixed layer (OML) model into the atmospheric model to link the temporospatial SST variability to oceanic mixing (Pollard et al., 1972; Davis et al., 2008; Wang and Duan, 2012; Price, 2009; Lin et al., 2013), and 3) coupling with an ocean model to provide a two-way air-sea interaction at the sea surface (Warner et al., 2010; Chen et al., 2013c; Lee and Chen, 2014; Lin et al., 2005; Lin et al., 2008; Lin et al., 2009; Wu et al., 2007; Wu et al., 2016). The first approach is the simplest and most straightforward to implement but does not include SST feedback to the ocean. Since the satellite-derived SST field is usually a daily product, it cannot resolve a rapid change in the ocean thermal condition beneath a storm over a daily cycle. The second approach considers the SST temporospatial variability by a one-dimensional (1-D) OML model. The Weather Research and Forecasting (WRF) includes two 1-D, temperature-dependent OML models developed by Pollard et al. (1972) and Price et al. (1986). Vertical mixing in Pollard et al.'s model was generated through turbulent shear and buoyancy productions by surface wind stress and cooling. Vertical mixing in Price et al.'s model (named PWP: Price-Weller-Pinkel) is determined by the criteria of turbulences parameterized by bulk shear instabilities. However, the 1-D OML models neglect the salinity contribution to the ocean stratification, horizontal advection in the ocean momentum and temperature fields, and Ekman pumping-induced surface cooling. Running the WRF-OML model requires the initial conditions of the SST and OML depth (Li et al., 2020). When a tropical storm moves onto the continental shelf, stratification could be changed significantly due to horizontal advection. This process, however, could not be resolved by a 1-D OML model (Dong et al., 2021).

Coupling WRF with an oceanic model is a straightforward solution with respect to improving marine boundary parameterizations, especially in resolving the physics of heat energy exchanges and wind-current-wave interaction processes attributing to surface roughness at the air-sea interfaces. Three popular oceanic models, the Princeton Ocean Model (POM), the Regional Ocean Modeling System (ROMS), and the MIT General Circulation Model (MITgcm), have been coupled with WRF or Hurricane WRF (HWRF) (Powers and Stoelinga, 1999;

Wilhelmsson et al., 2004; Seo et al., 2007; Warner et al., 2010; Yablonsky et al., 2015; Sun et al., 2019). All three oceanic models use structured grids. POM was initially coupled with MM5 (Powers and Stoelinga, 1999) and then with HWRF (Yablonsky et al., 2015). ROMS was coupled with WRF through a Model Coupling Toolkit (MCT) and named 'COAWST' (Warner et al., 2010). Mooney et al. (2016) applied COAWST to examine the influence of air-sea interactions on the intensity and trajectory of Hurricane Irene in the Atlantic Ocean. MITgcm was coupled with WRF through ESMF (Earth System Modeling Framework) and applied for simulating extreme heat events on the eastern shore of the Red Sea in 2012 (Sun et al., 2019). Sun et al. (2020) coupled the Climate extension of WRF (CWRF) with the unstructured-grid, Finite Volume Community Ocean Model (FVCOM) for the Great Lakes.

When a TC moves over a warm ocean surface, a cold wake could be generated behind that cyclone. The formation of a cold wake depends on water stratification in the pre-storm condition (Dong et al., 2021). In the cases of cold wake, the cooling can be up to 9°C and last for a few hours to more than a week (Lin et al., 2003; Wu et al., 2007; Dong et al., 2021). The cold wake could be formed by two mechanisms: Ekman pumping and vertical mixing. Pumping-induced upwelling is a latitude-dependent, vertical motion with an inertial time scale ($T_f = 2\pi/f$) (Greenspan, 1968; Frank, 1987). Over the northeastern continental shelf, T_f is in a range of 18.6–16.9 h at latitudes from 40° to 45° . Usually, a TC moves fast toward the coast with a few hours in this region, so Ekman pumping-induced surface cooling is unlikely to impact the storms substantially. However, inertial pumping due to resonance could occur on the right side of the storm center where the wind rotating frequency is close to the local inertial frequency (Price, 1981, 1983). This process could significantly intensify the cold wake in the maximum wind zone on the right side and thus cause a vital asymmetric SST feedback to the storm. Vertical mixing can be triggered by either turbulent shear and buoyancy production-induced diffusion processes or static or buoyancy instability-induced free convection and storm moving-induced forced convection (Schlichting, 1979). The diffusion and convection are characterized by time scales of $T_D \sim (h_m)^2/K_h$ and $T_v \sim h_m/w$, respectively (h_m is the mixed layer depth, K_h is the vertical thermal diffusion coefficient, and w is the vertical velocity). In general, the diffusion process has a much longer time scale than convection. In most ocean models, mixing is parameterized by diffusion coefficients

through turbulence closure schemes considering the influence of convection on turbulence productions (Mellor and Yamada, 1982; Chen and Beardsley, 1995; Burchard, 2002). Implementing a turbulent closure model into a primitive equation ocean model indirectly takes convection into account for vertical mixing. However, convection/overturbing is a kinematic process unresolvable in a hydrostatic (H) ocean model.

The non-hydrostatic (NH) convection is resolvable only in the motion in which the ratio of vertical to horizontal scales is $O(1)$ (Pedlosky, 1986). Marshall et al. (1997) reviewed the oceanic physical processes based on the motion scale. Based on their classifications, the vertical convection scale is $O(1.0 \text{ km})$. This scale applies to the deep-water formation but not the coastal ocean. Over the U.S. northeast shelf, the water depth ranges from a few meters to $\sim 200 \text{ m}$. To fully resolve the NH process, it requires a model configured with a horizontal resolution of $\sim 200 \text{ m}$ or less. On the other hand, the water is mixed vertically in the near-shore area ($h_m \sim D$, where D is the water depth), especially during a storm passage. In this area, the turbulent diffusion scale could be close to or the same as the convection scale, making it difficult to distinguish and evaluate the roles of the convection process in vertical mixing.

Many studies have been conducted to examine the NH processes for the formation and dissipation of high-frequency internal waves (e.g., Beji and Nadaoka, 1994; Lai et al., 2010a, 2010b, and 2019) and the convection induced by ice formation or high-rate evaporation at the sea surface (e.g., Jones and Marshall, 1993). Few studies have simulated tropical storms using a coupled NH atmosphere–ocean model. Currently available open-source coupled atmospheric and ocean models are discretized on a structured grid. The structured-grid models have successfully simulated the air-sea interaction processes in the regional ocean. However, the inflexibility in grid-refinement and geometric fitting around the vicinity of steep topography limit their applications to storm-induced coastal inundation.

Oceanic responses to tropical cyclones are characterized by the so-called “forced” and “relaxation” stages (Price et al., 1994). In the forced stage, in addition to wind-induced vertical mixing, the formation on the right side of a storm could be due to resonant responses of ocean currents to inertial wind variation (Price, 1981). When a storm passes a location, the wind rotates clockwise on the right and anticlockwise on the left side. When the clockwise rotation is close to the local inertial period, it could cause strong inertial currents in the upper OML, producing an intense cold wake on the right side. The turning rate of wind stress is related to the storm translation speed and size, which is often observed in a tropical storm with a high translation speed of $> 6 \text{ m/s}$ (Price et al., 1994). The relaxation stage is a period during which storm-induced energy is dispersed and dissipated through internal inertial waves after the storm passes (Price, 1983; Chen and Qin, 1985a, 1985b). As baroclinic responses, inertial-internal waves are generated underneath a moving storm (Price, 1983). In the horizontal, the wavelength of internal inertial waves approximately equals 95% of the product of the inertial period and storm translation speed along the storm track. It has the same scale as the storm size in the cross-storm direction. The storm energy also disperses vertically, with a scale deeper than the OML thickness. The storm energy decays rapidly after its energy is transferred from the upper OML into the thermocline.

In view of the foregoing discussions, we coupled WRF with FVCOM. FVCOM incorporates hydrostatic and nonhydrostatic dynamics (Chen et al., 2003; Chen et al., 2006; Chen et al., 2013b; Lai et al., 2010a, b). It is an unstructured-grid model flexible to refine the grid around the hurricane center tracks with more computational efficiency when a non-hydrostatic option is selected. The coupled WRF-FVCOM can promote the FVCOM application for the multi-scale air-sea interaction processes. We have applied this coupled model to verify and quantify the roles of oceanic processes in the development and movement of Hurricane Sandy over the U.S. northeastern shelf. Is the two-way air-sea interaction critical in predicting the intensity and path of Sandy? Is the left-side intensified asymmetric wind field observed in Hurricane Sandy related

to the oceanic heat energy transfer? Could the storm-induced heat exchange at the air-sea interface beneath a storm substantially differ when the NH process turns on? If it does, does the NH process matter for the hurricane simulation? Did the inertial resonance occur during the Sandy crossing? What level of difference did the resonance response attribute to storm-induced vertical mixing and convection? These questions are examined by comparing the non-hydrostatic and hydrostatic coupled WRF-FVCOM models in this study.

The remaining sections are organized as follows. Section 2 first introduces the coupled WRF-FVCOM, including its components and coupling framework, and then describes the experimental designs for Sandy simulation and the observed data for the model validation. Section 3 compares the model results versus observations. Section 4 discusses the feedback contributions of oceanic processes to Sandy’s winds, air pressure, path, and oceanic responses to Sandy under hydrostatic and non-hydrostatic dynamic conditions. Section 5 summarizes the major findings. This paper includes two appendices, which discuss the restriction in the time step in a non-hydrostatic ocean model and derives the relationship between the storm translation speed and inertial resonance radius.

2. The Model, experimental Designs, and data

2.1. The coupled WRF-FVCOM model

FVCOM was coupled with WRF (hereafter referred to as WRF + FVCOM) through the Earth System Model Framework (ESMF). The objective of developing this coupled model was to 1) improve both atmosphere and ocean models by implementing the air-sea interaction dynamics at the sea surface through the data exchanges between these two models and 2) provide the geoscience community with an alternative structured and unstructured-grid coupled atmosphere–ocean model system including either hydrostatic or non-hydrostatic processes. An effort was made not only to develop a workable coupled model but also to create a user-friendly coupled code that could be easily configured and run for process-oriented experiments, hindcast simulations, and forecast operations. The coupled model can parallelly run and execute in the concurrent mode. Multiple interpolation methods were implemented to support the data exchange between structured and unstructured grids.

WRF + FVCOM consisted of three modules: the atmosphere component (WRF), the ocean component (FVCOM), and the coupler (ESMF). WRF and FVCOM can be run separately as subroutines in the coupled system. ESMF acted as a bridge to transfer the data between WRF and FVCOM and a controller to execute the coupled model operation. Structures of WRF, FVCOM, and ESMF are briefly described as follows.

WRF is a structured-grid, primitive equations, mesoscale atmosphere model developed by a collaborative group of the National Center for Atmospheric Research (NCAR), the National Centers for Environmental Prediction (NCEP), the U.S. Air Force, the Naval Research Laboratory, the University of Oklahoma, and the Federal Aviation Administration (FAA) (Skamarock et al., 2008). WRF has been widely used for regional forecast and hindcast operations, with the initial and boundary conditions from the GFS (the Global Forecast System), the NCEP FNL (Final) Operational Global Analysis Data, or the European Centre for Medium-Range Weather Forecasts (ECMWF). The governing equations in WRF are discretized using the Arakawa-C grid in the horizontal and a hybrid sigma-pressure vertical coordinate in the vertical (Park et al., 2013). It is solved numerically using the time-split integration scheme with the third-order Runge-Kutta method. WRF also contains three-or four-dimensional variational data assimilation (3DVAR or 4DVAR) algorithms and has options to couple with air chemistry (Grell et al., 2005) and hydrological models (Gochis et al., 2020). Currently, there are two open-source WRF codes available: 1) the Advanced Research WRF (ARW) developed and upgraded by NCAR and 2) the Nonhydrostatic

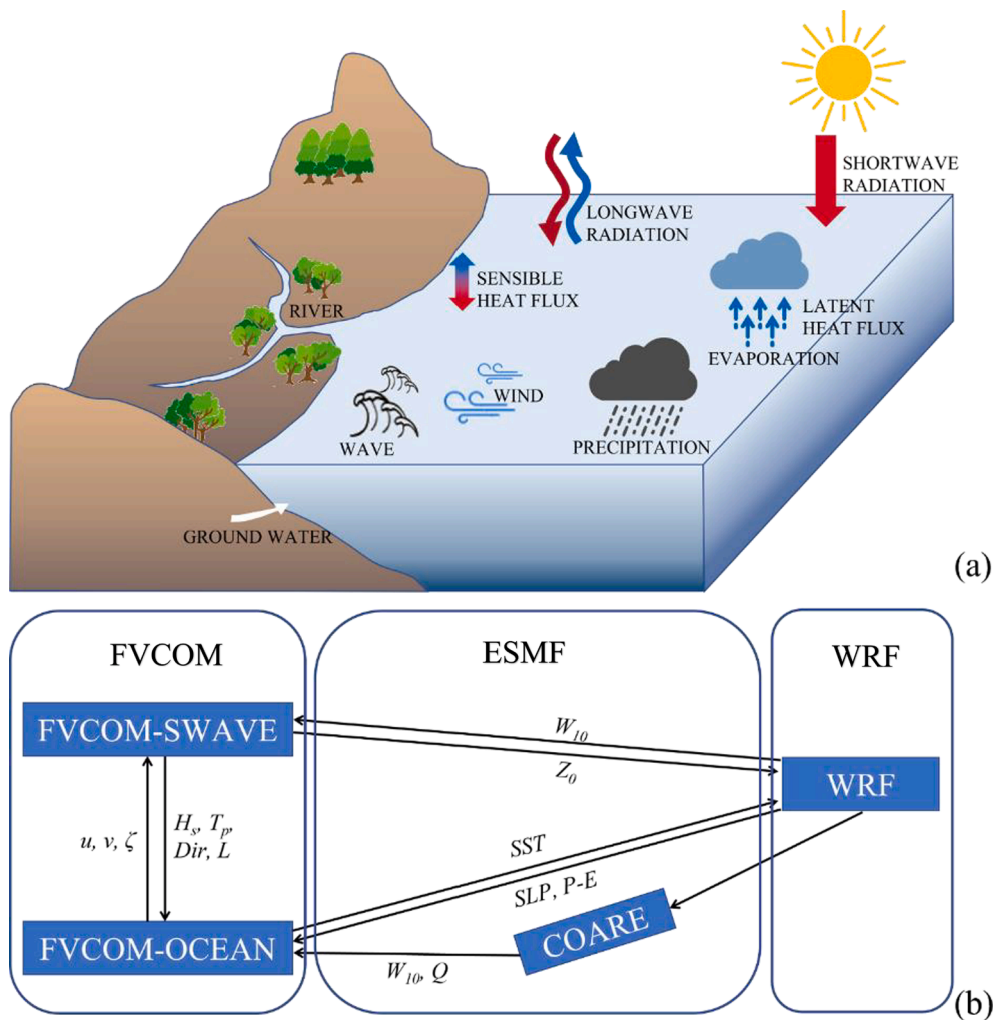


Fig. 2. Illustration of exchange processes of atmospheric, oceanic, and wave variables and parameters at the air-sea interface between WRF and FVCOM.

Mesoscale Model (NMM) by NCEP. Version 4.3.3 of ARW is used to couple with FVCOM (https://www2.mmm.ucar.edu/wrf/users/download/get_sources_new.php, last access: Mar. 2022). ARW is referred to as “WRF” in this manuscript as consistent terminology.

FVCOM is a prognostic, three-dimensional (3D), free surface, primitive equation, ocean model developed by the collaborative partnership of the University of Massachusetts, Dartmouth (UMASS-Dartmouth), and the Woods Hole Oceanographic Institution (WHOI). It has been upgraded by the development team with contributions from user communities (Chen et al., 2013a). The governing equations of FVCOM encompass both hydrostatic and non-hydrostatic dynamics (Lai et al., 2010a, b) in the Cartesian or spherical coordinate system with options to couple surface waves (FVCOM-SWAVE, Qi et al., 2009), sea ice (Gao et al., 2011), non-cohesive and cohesive sediments (Chen et al., 2013b; Ge et al., 2020), low tropical food web dynamics (Chen et al., 2013b; Tian et al., 2015). The equations are discretized using unstructured, non-overlapped triangular grids in the horizontal and a generalized, spatially-varying terrain-following coordinate in the vertical. The unstructured grid accurately fits irregular coastal geometries and has flexibility in refining the grid over steep continental margins, ridges, and islands. The terrain-following vertical coordinate is designed to fit the bottom topography. The spatial fluxes of momentum are discretized using a second-order accurate finite-volume method (Kobayashi et al., 1999). Spatial fluxes of scalars (e.g., temperature, salinity) are computed using a second-order accurate finite-volume upwind scheme (Chen et al., 2013b) or total variational diminishing (TVD) scheme (Darwish

and Moukalled, 2003) through conjunction with a vertical velocity adjustment to enforce exact conservation of the scalar quantities. A Smagorinsky formulation (Smagorinsky, 1963) is used to parameterize horizontal diffusion, and turbulent vertical mixing is calculated using the General Ocean Turbulence Model (GOTM) libraries (Burchard, 2002), with the 2.5 level Mellor-Yamada (1982) turbulence model used as the default. A wet/dry point treatment method simulates the flooding/drying processes over intertidal zones and storm-induced coastal inundation (Chen et al., 2008). FVCOM is solved numerically by either a mode-split (like POM and ROMS) (Chen et al., 2003) or a semi-implicit integration method (Lai et al., 2010a) under the Message Passing Interface (MPI) (Cowles, 2008). FVCOM contains multiple data assimilation methods, including 4-D nudging, optimal interpolation (OI), and Kalman Filters (Chen et al., 2009). The multiple nesting modules, including ESMF, were implemented to integrate either multi-domain FVCOM domains or other unstructured/structured grid models (Chen et al., 2013b; Qi et al., 2018). Version 4.1 of FVCOM is used in this study (<http://fvcom.smast.umassd.edu/>, last access: Oct. 2020), which was released to the public in 2019.

ESMF defines an architecture for composing complex, coupled modeling systems and includes data structures and utilities for developing individual models (Hill et al., 2004). The basic idea behind ESMF is that complicated applications can be divided into smaller pieces or components. A component is a software composition unit with a coherent function and a standard calling interface and behavior. Components can be assembled to create multiple applications, and different

Table 1

Experiment descriptions. For ocean dynamics column, 'H' for hydrostatic and 'NH' for non-hydrostatic.

Case	Model	Ocean dynamics	Meteorological forcings	Oceanic forcings
WRF + FVCOM-NH	Coupled model	NH	Via coupler	Via coupler
WRF + FVCOM-H	Coupled model	H	Via coupler	Via coupler
WRF	WRF	\	\	Static FNL data
FVCOM-NH	FVCOM	NH	From WRF	\
FVCOM-H	FVCOM	H	From WRF	\

implementations of a component may be available. In ESMF, a component may be a physical domain or a function such as a coupler or an I/O system. ESMF also includes toolkits for building components and applications, such as re-gridding software, calendar management, logging and error handling, and parallel communications. Two models or more, no matter whether they are in a structured grid or unstructured grid, can be coupled in either a one-way or two-way framework. The version of ESMF presented in this work is 8.0.1 (https://github.com/esmf-org/esmf/releases/tag/ESMF_8.0.1, last access: Oct. 2020).

Multiple dynamic processes are implemented to capture the interaction at the air-sea interface in the WRF-FVCOM (Fig. 2a). Four variables are passed from the atmosphere to the ocean: wind stress, heat flux, precipitation minus evaporation, and sea level pressure. Meanwhile, the ocean provides SST to the atmosphere as a bottom boundary condition. When the surface waves are considered, the wind stress is calculated with wave parameters. The marine boundary parameterization in WRF accounts for the influences due to wave-induced ocean surface roughness. This ocean surface roughness is a function of the significant wave height, wavelength, and wave period. The two-way communication is illustrated conceptually in Fig. 2a with variables listed in Fig. 2b. Variables and parameters in data exchanges between the two models are described and discussed as follows.

The wind stress used in WRF + FVCOM is defined as $\vec{\tau} = \rho_a C_d |\vec{v}_{10} - \vec{v}_0| (\vec{v}_{10} - \vec{v}_0)$, where $\vec{\tau}$ is the wind stress vector, ρ_a is the air density, C_d is the drag coefficient, \vec{v}_{10} is the 10-m wind speed vector, and \vec{v}_0 is the surface ocean velocity vector. $\vec{v}_{10} - \vec{v}_0$ is defined as the relative wind vector. The difference between the relative and absolute wind speeds is relatively small since surface ocean currents are generally one order of magnitude smaller than the wind velocity (Duhaut and Straub, 2006). However, the surface currents could change the relative wind direction and modify the ocean surface energy input through friction and ocean mesoscale eddy dissipation (Dewar and Flierl, 1987), leading to an underestimation in C_d when the surface currents are > 0.5 m/s (Edson et al., 2013). It could account for a 20%-35% overestimation of the wind energy into the ocean (Duhaut and Straub, 2006). In addition to the default setup based on Large and Pond's formulation (Large and Pond, 1981), WRF + FVCOM implements three different ocean surface roughness (Z_0) parameterization equations, 'TY2001' (Taylor and Yelland, 2001), 'DGHQ' (Drennan et al., 2003), and 'OOST' (Oost et al., 2002). TY2001 considers the influence of wave steepness, DGHQ includes the wave age's effect, and OOST takes both the wave age and steepness into account, with the formulations given as.

$$TY2001 : Z_0 = 1200 \left(\frac{H_s}{L_p} \right)^{4.5} H_s$$

$$DGHQ : Z_0 = 3.35 \left(\frac{u_*}{c_p} \right)^{3.4} H_s$$

$$OOST : Z_0 = \frac{25}{\pi} \left(\frac{u_*}{c_p} \right)^{4.5} L_p$$

where H_s is the significant wave height; L_p is the peak wavelength; c_p is the wave phase speed; and u_* is the wind friction velocity. H_s , L_p , and c_p are collected from FVCOM-SWAVE, and u_* is calculated in the COARE (Coupled Ocean-Atmosphere Response Experiment) algorithm (Fairall et al., 1996; Chen et al., 2005). In the Hurricane Sandy experiments, the wave module was not turned on.

Chen et al. (2005) compared the MM5 (later WRF) outputs of sensible and latent heat fluxes with observations on the southern flank of Georges Bank. They found that these fluxes could be largely overestimated during a storm period. The errors could be corrected by recalculating heat fluxes using COARE 2.6 or over. The COARE 2.6 and 4.0 were implemented in the WRF + FVCOM. In WRF, the precipitation rate (P) was an accumulated variable composed of cumulus precipitation (RAINC), grid-scale precipitation (RAINNC), and shallow cumulus precipitation (RAINSH) (Skamarock et al., 2008). The shallow cumulus precipitation was produced by warm rain showers from shallow cumuli (Nuijens et al., 2009). These three kinds of precipitations could be determined using the cumulus and microphysics schemes coded in WRF. WRF didn't output evaporation rate (E). E was calculated using the SST from FVCOM and the latent heat flux from the COARE algorithm.

2.2. Experimental designs

Hurricane Sandy was selected as an example to study 1) the impact of air-sea interactions on its intensity and path and 2) oceanic responses to Sandy under hydrostatic and non-hydrostatic conditions. Five experiments are designed as listed in Table 1. The WRF + FVCOM simulation experiments covered the period from 00:00 28 Oct. 2012 to 00:00 31 28 Oct. 2012, during which the storm moved across the Mid Atlantic Bight (Fig. 3). The experiments were done with H and NH processes. To quantify the importance of the two-way air-sea coupling, we also conducted the experiments using uncoupled WRF, FVCOM-H, and FVCOM-NH.

The WRF + FVCOM experiments were done using the Northeast Coastal Ocean Forecast System (NECOFS) grid configuration (Chen et al., 2021b). In NECOFS, WRF consisted of three two-way nested domains with the horizontal resolution of 27 km, 9 km, and 3 km, respectively (Fig. 3a). The time steps used in these three domains were 120, 40, and 13.33 s, which were determined to satisfy the Courant-Friedrichs-Lowy (CFL) condition. Thirty-six vertical sigma levels were set with the top minimum pressure of 50 hPa. We tested the WRF performance for Sandy simulation with various cumulus parameterizations, planetary boundary layer (PBL) schemes, and grid design/resolution (Li et al., 2020). The best results were achieved with a 3-km resolution, the Mellor-Yamada-Janjić (MYJ) scheme (Janjić, 1994) for PBL parameterization, and the Tiedtke scheme (Tiedtke, 1989) for the cumulus calculation (Li et al., 2020). The Tiedtke scheme was only applied for domains 1 and 2 since WRF could solve convection as the resolution is less than 4 km (Jeworrek et al., 2019). The initial condition and boundary forcing for WRF were from the FNL dataset, with a 1-degree resolution and 6-hour time interval. No data assimilation was executed. In the WRF + FVCOM experiments, the OML module in WRF was turned off, and the SST was transferred directly from FVCOM at every WRF's domain-1 time step (120 s).

The ocean model used in this study was FVCOM-GOM3 in NECOFS (Chen et al., 2021b), with the computational domain covering the region from the south end of Delaware Bay to the Nova Scotian Shelf (Fig. 4). The horizontal resolution varied from ~ 40 km in the open ocean to ~ 200 m in the coastal region and shelf break. A hybrid terrain-following coordinate was used in the vertical. In the region where depth is shallower than 225 m, the σ -coordinate with a uniformly level interval was set. In the area where depth is deeper than or equal to 225 m, the s -coordinate was applied, with a uniform thickness of 5 m in the upper 5 layers from the surface and 3 layers above the bottom. The transition between σ - and s -coordinates was at the 225-m isobath, at which all

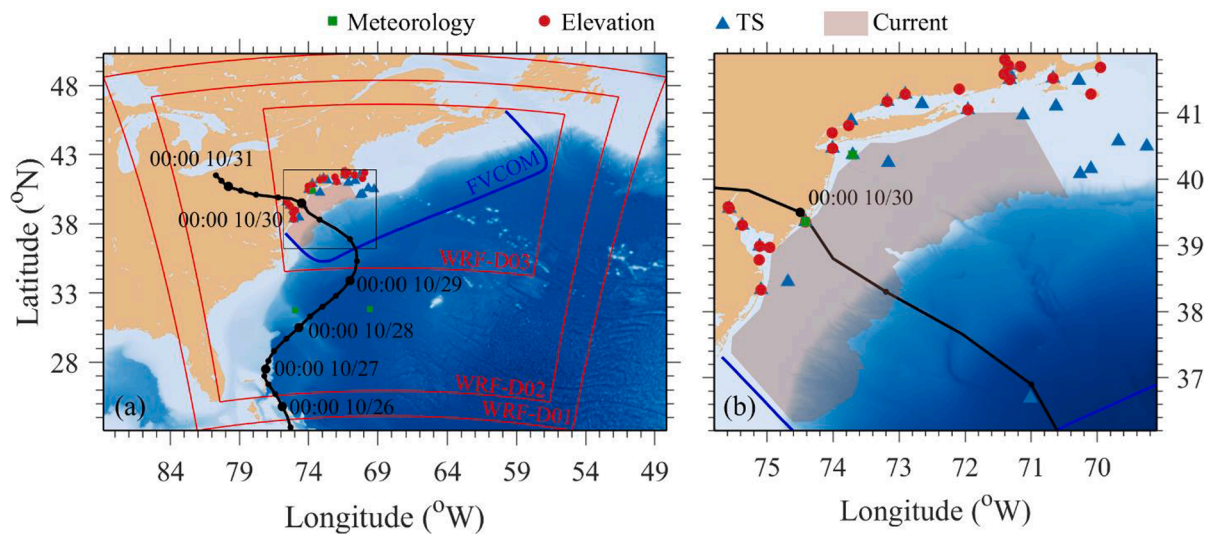


Fig. 3. (a): the WRF (red lines) and FVCOM (blue lines) domains, the trajectory of Hurricane Sandy (black lines), the locations of meteorological buoys (filled green squares), tidal gauges (filled red dots), and temperature/salinity measurement sites (filled blue triangles), and the covered region of the HFR Array (the shadow area). WRF encompasses three two-way nested domains with horizontal resolutions of 27 (D01), 9 (D02), and 3 (D03) km. Numbers with the hurricane trajectory are hours: minutes, months/days. (b): An enlarged view of the boxed area in (a).

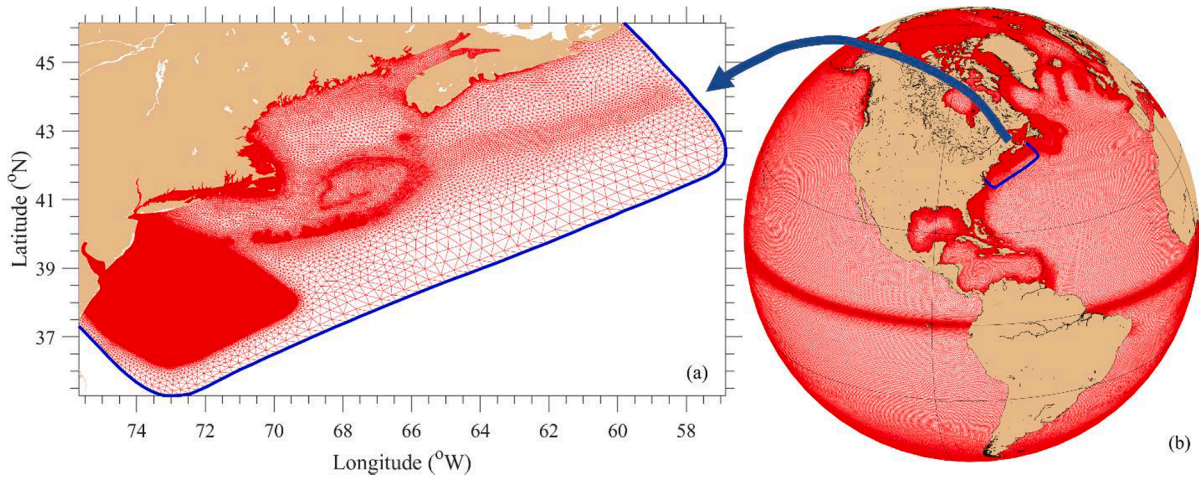


Fig. 4. The FVCOM (a) and Global-FVCOM (b) triangular grids. The blue line in the right and left panels is the nesting boundary between the global and regional models. The finest resolution is 0.3–2.0 km in FVCOM and 2 km in Global-FVCOM.

layers had a uniform thickness of 5 m. The hybrid coordinate approach could avoid the numerical bias in simulating the surface ocean mixed and bottom boundary layers. FVCOM-GOM3 is a one-way global and regional nested model system with the open boundary condition consisting of tidal and low-frequency subtidal elevations plus the low-frequency subtidal currents, temperature (T_s), and salinity (S) (Fig. 4). The elevation encompassed six tidal constituents (M_2 , N_2 , S_2 , O_1 , K_1 , P_1), and the low-frequency subtidal variables at the nesting boundary were provided by the Global-FVCOM hindcast simulation results (Chen et al., 2016; Zhang et al., 2016). FVCOM-GOM3 includes 49 rivers at the coastal cells with freshwater discharges specified using the USGS (U.S. Geological Survey) data. No data assimilation was performed in the Hurricane Sandy simulation.

Hurricane Sandy entered the FVCOM-GOM3 domain at around 03:00 on 29 Oct. 2012 and made its landfall at 23:30 on 29 Oct. 2012. The FVCOM-GOM3 grid covered the hurricane maximum wind zone. We refined the FVCOM-GOM3 grid in the max-wind zone around the storm center track to ~ 2 km (Fig. 4a). The simulation was conducted with the understanding that the refined grid does not satisfy the $O(1)$ vertical–horizontal scale ratio criterion for a fully NH application. Despite that,

turning on the NH process in WRF + FVCOM could still be used to examine the numerical performance of the coupled WRF + FVCOM-NH for storm simulation. The vertical velocity in an H ocean model is determined by the incompressible continuity equation. The vertical velocity in an NH ocean model is calculated directly from the vertical momentum equation. In addition to buoyancy forces, it is also affected by vertical viscosity, horizontal momentum diffusion, and nonlinear advection. Regarding vertical convection, a ~ 1 -km resolution ocean model leads to $O(1)$ and $O(10^{-1})$ ratios of the vertical to horizontal scales in the deep and slope areas. Although the WRF + FVCOM-NH didn't fully resolve convection in the shallow area in our experiments, it could still provide a lower-order approximate NH feature over the slope through the comparison with the hydrostatic WRF + FVCOM. Both the H and NH FVCOMs were run using the same refined grid.

In the WRF + FVCOM simulation, the model was run with the FVCOM initial condition specified using the assimilated hindcast fields at 00:00 on 28 Oct. 2012. NECOFS has saved daily restart files covering the period 1978–2020, which allows us to run WRF + FVCOM with no requirement for a ramp time. In all experiments, FVCOM-GOM3 was solved using a semi-implicit with time steps of 2 s for non-hydrostatic

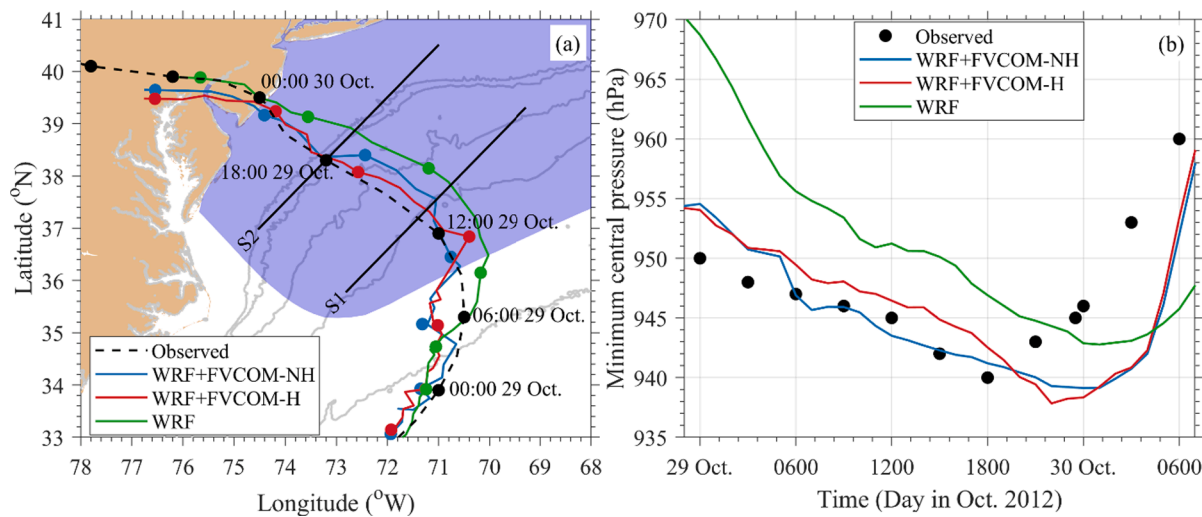


Fig. 5. Comparisons between the simulated and observed paths of Hurricane Sandy (a) and minimum central pressures (b) for the WRF + FVCOM-NH (blue lines), WRF + FVCOM-H (red lines), and uncoupled WRF (green lines) cases. In (a), the shaded area is the FVCOM domain; the solid black lines labeled “S1 and S2” are the transects used in Fig. 12 and Figs. 18–23.

Table 2

Comparisons between the simulated and observed paths of Hurricane Sandy and minimum central pressures for the WRF + FVCOM-NH, WRF + FVCOM-H, and uncoupled WRF cases. The time was from 18:00 on 28 Oct. to 21:00 on 29 Oct. ΔD_{max} : the maximum center distance; $RMSE_D$: the root-mean-square error of center location; ΔSLP_{max} : the maximum error of central SLP; $RMSE_{SLP}$: the root-mean-square error of central SLP.

Variables	WRF + FVCOM-NH	WRF + FVCOM-H	WRF
ΔD_{max} (km)	78.5	94.7	255.5
$RMSE_D$ (km)	57.1	47.6	193.7
ΔSLP_{max} (hPa)	6.9	6.7	25.2
$RMSE_{SLP}$ (hPa)	3.9	4.2	12.2

cases and 20 s for H cases. More details of the time step selection for NH cases are presented in Appendix A.

2.3. The data

The WRF-FVCOM simulation results were compared with available observations (Fig. 3), including 1) the time series of the hurricane center location, minimum pressure, and maximum wind downloaded from the NCDC International Best Track Archive for Climate Stewardship (IBTrACS) project database (Knapp et al., 2010), 2) the wind and pressure data at four meteorological buoys (#44065, ACYN4, 41,048 and 41,002) collected from the National Data Buoy Center (NDBC) (<https://www.ndbc.noaa.gov/>), 3) the water elevations at 23 tidal gauges with hourly sea-level records from NOAA Tides and Currents database (<https://tidesandcurrents.noaa.gov/>), 4) the T_s and S data from NDBC, the Northeast Fisheries Science Center (NEFSC), and the National Oceanographic Data Center (NODC), and 5) the 6-km resolution, hourly coastal surface currents were observed via the 22-station High Frequency Radar (HFR) array network (Roarty et al., 2020) from the Mid-Atlantic Regional Coastal Ocean Observing System (MARACOOS). The data were downloaded from https://hfrnet-tds.ucsd.edu/thredds/HFRADAR_USEGC.html.

Four meteorological buoys were within the radius of the maximum wind zone of Hurricane Sandy. 41,048 and 41,002 are located in the open ocean, while ACYN4 and 44,065 are near the coast. The wind sensors on Buoy ACYN4 did not function well during the Sandy crossing. When Hurricane Sandy traversed toward the coast, the minimum distance of Buoys 44065, ACYN4, 41002, and 41,048 to the hurricane center were 118.1, 12.0, 108.6, and 241.3 km. The 23 tidal gauges were

all in the Sandy's influenced area from Cape Cod to Delaware Bay. The NDBC surface T_s and S data used in this study were from the measurements at 12 stations in the FVCOM-GOM3 domain. The mapping data of surface currents covered the coastal area from Cape Cod to Cape Hatteras. Starting from 17:00 on 29 Oct. 2012, >40% of data were unavailable due to high winds. We only compared the model-simulated surface currents with the data from 00:00 28 Oct. 2012 to 16:00 29 Oct. 2012.

3. Model-data Comparisons

3.1. Meteorological observations

a) Hurricane center track and intensity.

The IBTrACS records showed that Hurricane Sandy entered the WRF D02 after 00:00 on 29 Oct. 2012, with a minimum sea level pressure (SLP) of 950 hPa. Starting from 09:00 on 29 Oct. 2012, it turned left and approached the coast as the center SLP dropped. At 18:00 on 29 Oct., the central SLP reached a minimum of 940 hPa when the hurricane traversed the continental shelf. The hurricane finally made its landfall near Atlantic City, New Jersey, at 23:30 on 29 Oct. The central SLP increased to 945 hPa as it landed. When it moved onto the land, the hurricane intensity rapidly decreased, with the minimum SLP increasing to 960 hPa in about 6 h.

For the case without air-sea coupling, the WRF-simulated hurricane started to depart from the observed path beginning 00:00 29 Oct. (Fig. 5a), and then moved in a different route on the eastern side of the observed track. The maximum deviation distance was 255.5 km, with a root-mean-square error (RMSE) of 193.7 km. The distinct modeled hurricane trajectory led to a substantial bias in the simulated central SLP (Fig. 5b). The simulated central SLP was 8.2 hPa higher than the observation at 06:00 on 29 Oct. Although the simulated central SLP also dropped as it approached the land, it was 3 ~ 6 hPa overestimated. As a result of the long traveling journey, the simulated hurricane landed with a 3-hour delay. The maximum SLP error from 18:00 on Oct. 28 and 21:00 on Oct. 29 before landfall was 25.2 hPa, with an RMSE of 12.2 hPa.

Activating the two-way air-sea interaction process, WRF + FVCOM substantially improved the hurricane simulation in both the center track and the intensity, especially after the hurricane entered the region where the air-sea coupling was executed with the fully overlapped atmosphere and ocean domains (Fig. 5). In this overlapped domain, the

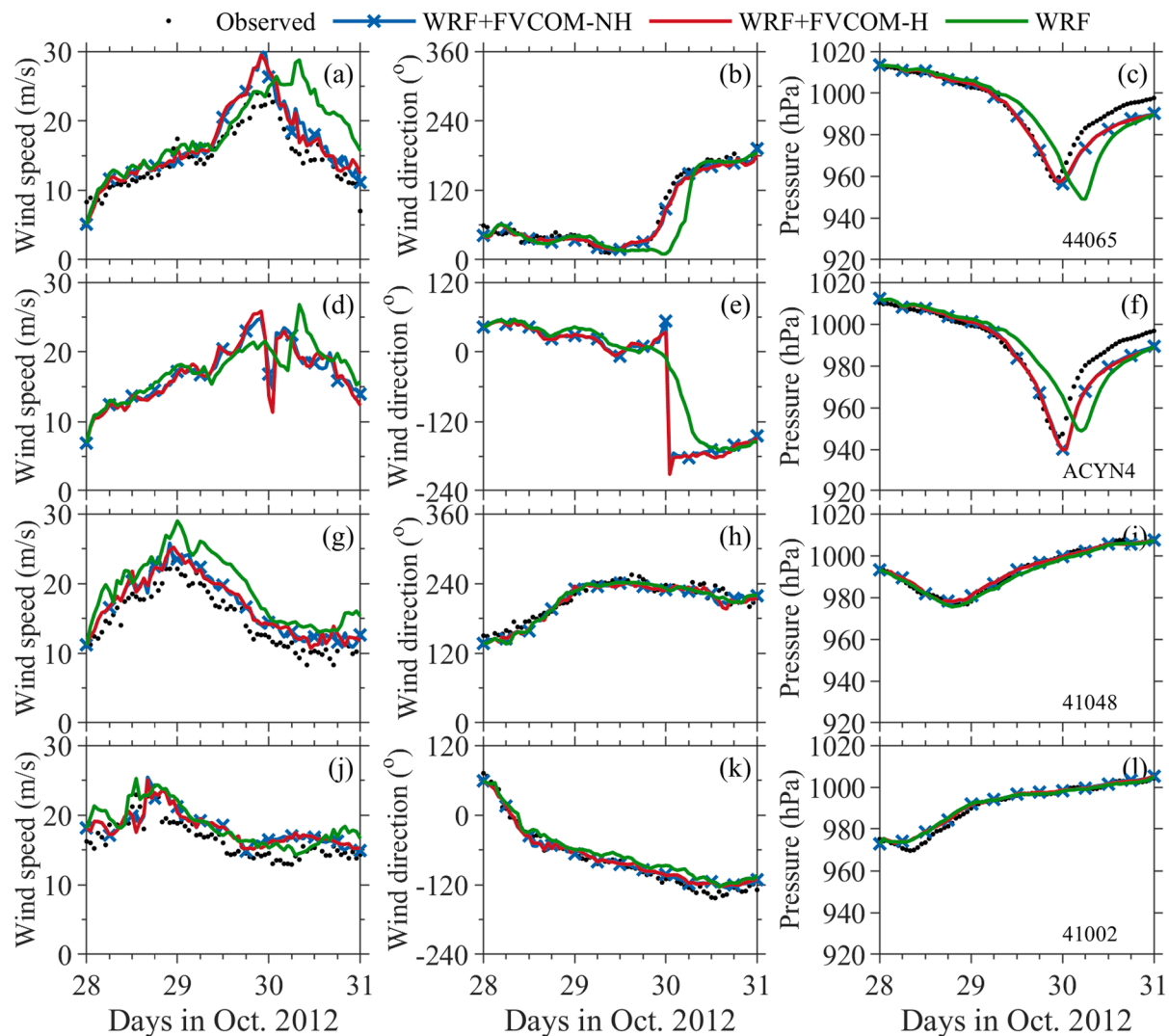


Fig. 6. Comparisons between the simulated and observed 10-m wind speeds, 10-m wind directions, and sea level pressures at buoy stations 44065, ACYN4, 41048, and 41,002 for the WRF + FVCOM-NH (blue lines), WRF + FVCOM-H (red lines) and uncoupled WRF (green lines) cases.

Table 3

Comparisons between the simulated and observed 10-m wind speeds, 10-m wind directions, and sea level pressures at buoy stations 44065, ACYN4, 41048, and 41,002 for the WRF + FVCOM-NH, WRF + FVCOM-H and uncoupled WRF cases. ΔWS_{max} : the maximum error of 10-m wind speed; $RMSE_{WS}$: the root-mean-square error of 10-m wind speed; ΔWD_{max} : the maximum error of 10-m wind direction; $RMSE_{WD}$: the root-mean-square error of 10-m wind direction; ΔSP_{max} : the maximum error of surface pressure; $RMSE_{SP}$: the root-mean-square error of surface pressure. Light blue box: the WRF + FVCOM-NH case; brown box: the WRF + FVCOM-H case; clear box: the uncoupled WRF case.

Stations	44065			ACYN4			41048			41002		
ΔWS_{max} (m/s)	7.8	7.8	13.6	-	-	-	4.8	4.2	7.4	4.5	3.9	6.1
$RMSE_{WS}$ (m/s)	2.8	2.6	5.0	-	-	-	2.3	2.2	4.7	2.1	2.0	2.5
ΔWD_{max} (°)	28.1	24.7	102.1	-	-	-	26.7	30.6	23.4	27.1	27.9	30.2
$RMSE_{WD}$ (°)	9.0	8.5	31.6	-	-	-	10.3	10.3	9.9	9.4	9.3	15.6
ΔSP_{max} (hPa)	9.7	7.5	34.1	17.4	12.1	30.0	2.8	2.9	3.0	5.6	5.7	5.3
$RMSE_{SP}$ (hPa)	4.7	4.1	11.3	6.1	5.0	11.9	1.2	1.2	1.4	2.0	2.0	2.0

simulated hurricane moved in a closed path to the observed track (Fig. 5a), with the maximum deviation distance from the observed path being dropped to 94.7 km in the H case and 78.5 km in the NH case, ~160 km smaller compared with the WRF case (Table 2). The RMSEs were 47.6 and 57.1 km for the coupled H and NH cases, respectively, showing an improvement of ~ 69 % compared with the WRF case. As for the intensity, WRF + FVCOM also performed better than WRF. Before the simulated hurricane entered the ocean model domain (prior to 06:

00 on 29 Oct.), its minimum central SLP was 4.1 hPa higher than the observed central SLP. This error rapidly dropped to ~ 1.7 hPa or less after entering the region where the two-way air-sea interaction activated. The RMSE of the SLP over the period before landfall was 4.2 and 3.9 hPa for the H and NH cases, which was ~ 8.2 hPa smaller than the uncoupled WRF case. The WRF performance for the SLP was improved by 66.8% after turning on air-sea coupling. In the WRF + FVCOM case, the simulated SLP rapidly escalated to 959 hPa after landing, while it

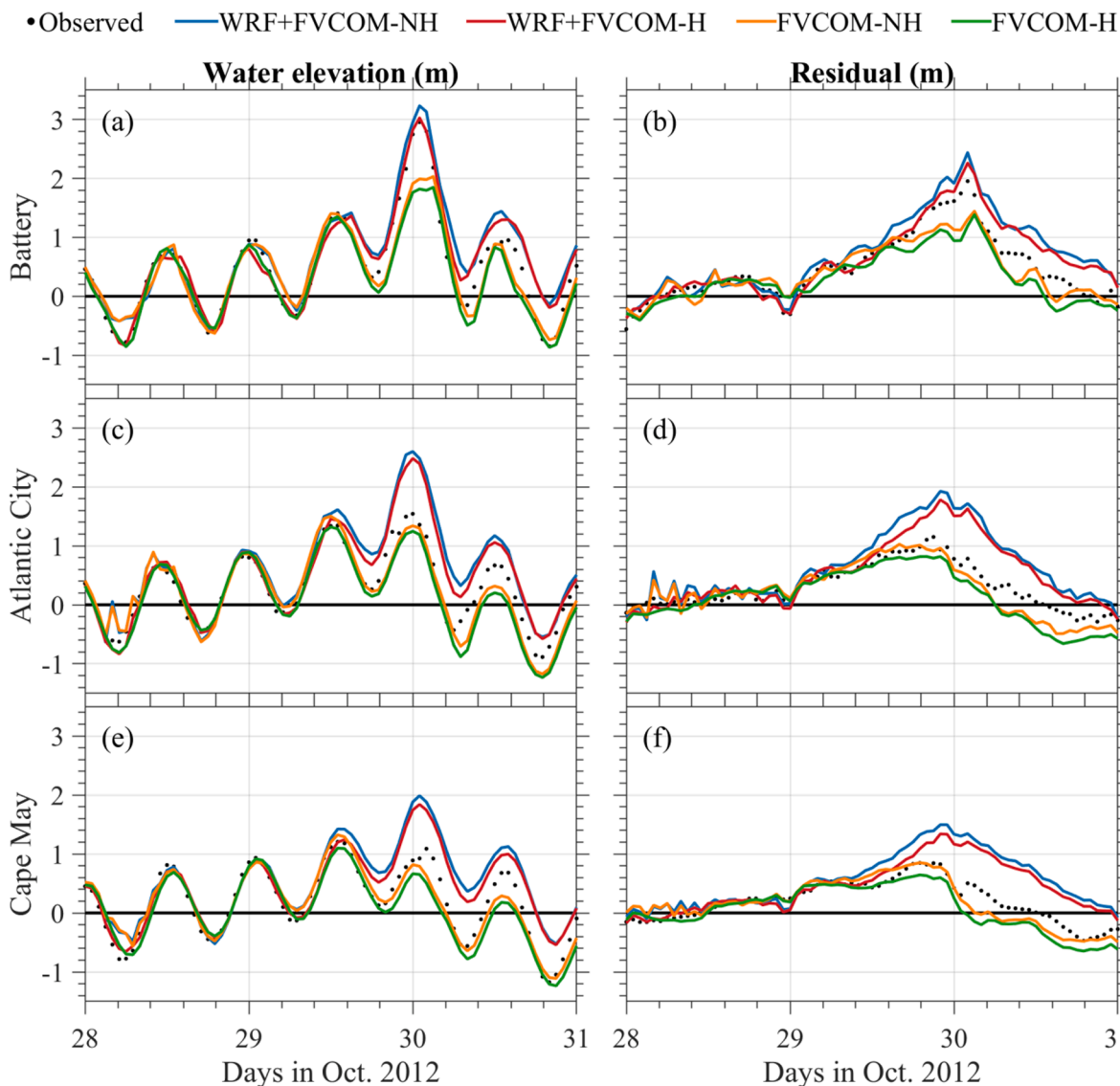


Fig. 7. Comparisons between the simulated and observed water elevations and residuals at tide gauge stations the Battery, Atlantic City, and Cape May for the WRF + FVCOM-NH (blue lines), WRF + FVCOM-H (red lines), FVCOM-NH (brown lines), and FVCOM-H (green lines) cases.

remained slightly changed in the uncoupled WRF case. The coupled model supplied more realistic marine boundary conditions than the static FNL data, which was critical to capturing a hurricane's intensity and path. WRF + FVCOM-NH did not substantially improve the Sandy track simulation compared with WRF + FVCOM-H (Fig. 5a). Although the maximum distance deviation was reduced in the NH case, its RMSE over the period before landfall increased by 16.6% (Table 2). Activating the NH process slightly reduced the RMSE in the SLP by 7.7% compared with the H case (Table 2).

b) Wind and surface pressure at buoys.

The observed 10-m wind speed, direction, and surface pressure at four buoys from NDBC were collected to evaluate the WRF model performance. WRF + FVCOM showed a better performance in the wind and pressure simulation than WRF (Fig. 6), showing RMSE reductions of 18–52% in wind speed and 40–72% in wind direction (Table 3). As a result of the improvement in the hurricane path, the coupled model reproduced the magnitude and timing of the wind speed peaks. WRF + FVCOM-simulated surface pressure also showed a better match to the observations. The uncoupled WRF resulted in a substantial bias of the

surface pressure at coastal buoys, with a mean RMSE of 11.6 hPa. This bias was reduced to 4.6 hPa in the WRF-FVCOM-H case and 5.4 hPa in the WRF-FVCOM-NH case (Table 5). In particular, the two-way air-sea interaction processes substantially improved the pressure simulation before landfall, especially in the timing of the pressure minimum, even though the pressure was underestimated after landfall. Due to the large northeastward deflection in the hurricane's track, the uncoupled WRF caused a ~ 6-h lag to reach the pressure minimum at the coastal buoys. The two coupled models performed similarly regarding the comparison results of the 10-m wind and the surface air pressure at coastal buoys. As aforementioned, the NH process was critical only when the ratio of vertical scale (H) to horizontal scale (L) was ~ 1. In our experiments, the finest grid resolution was about 2 km in the hurricane track areas over the shelf. The H/L ratio near the coast was much smaller than 1. The NH contribution to the water level, currents, and winds was only accounted for at a first-order approximation level. That was probably one of the reasons why the ocean simulation results did not differ much between the H and NH coupled cases.

Table 4

Water elevation RMSEs of the WRF + FVCOM-NH, WRF + FVCOM-H, FVCOM-NH, and FVCOM-H cases, at three selected stations and total 23 stations.

Station	WRF + FVCOM-NH (m)	WRF + FVCOM-H (m)	FVCOM-NH (m)	FVCOM-H (m)
The Battery	0.35	0.28	0.30	0.33
Atlantic City	0.47	0.38	0.23	0.26
Cape May	0.48	0.40	0.20	0.25
Total 23 stations	0.38	0.31	0.26	0.28

Table 5

Comparison of the surface current speed and direction for the WRF + FVCOM-NH, WRF + FVCOM-H, FVCOM-NH, and FVCOM-H cases. ΔCS_{mean} : mean current speed difference; ΔCS_{STD} : standard deviation of the current speed difference; ΔCD_{mean} : mean current direction difference; ΔCD_{STD} : standard deviation of the current direction difference; $RMSE_C$: RMSEs of the oceanic surface current vectors.

Variables	WRF + FVCOM-NH	WRF + FVCOM-H	FVCOM-NH	FVCOM-H
ΔCS_{mean} (m/s)	0.2	0.2	0.2	0.1
ΔCS_{STD} (m/s)	0.3	0.2	0.3	0.2
ΔCD_{mean} (°)	25.4	23.4	32.4	28.9
ΔCD_{STD} (°)	36.3	33.1	39.8	35.0
$RMSE_C$ (m/s)	0.4	0.3	0.4	0.3

3.2. Oceanic observations

a) Water elevation.

The simulated water elevations were compared with observed records at the 23 NOAA tidal gauges. There were 10 stations located within Sandy's maximum wind zone. Atlantic City was only 11.9 km away from the landfall position. Two stations, Cape May and Battery, located on the left and right sides of the hurricane track, were selected for the detailed comparison. For the overall performance, at Battery, the simulated water levels were better in the coupled cases than those in the uncoupled cases (Fig. 7a and b). At Atlantic City and Cape May, the uncoupled cases' water levels were close to the observation. WRF + FVCOM predicted higher surges at the coast than the uncoupled FVCOM during the Sandy crossing, especially at stations within the Sandy maximum wind zone (Fig. 7). In the first one and half days, when the hurricane was still far from the coast, the water elevations produced by uncoupled and coupled FVCOMs were similar, matching the observations well. The simulated water elevations began to diverge as the hurricane was close to the coasts and passed. The coupled model-simulated surge was overestimated by ~ 0.14 m, with an RMSE of 0.31 m (H) and 0.38 (NH). In comparison, the uncoupled model-simulated surge presented an underestimation of ~ 0.10 m, with an RMSE of 0.28 m (H) and 0.26 (NH) (Table 4). The residual was calculated by removing tidal signals from harmonic analysis (Fig. 7: right panels). The peak time of the surge was all accurately captured by uncoupled and coupled FVCOMs. The NH-coupled model predicted a slightly higher surge than the H-coupled model.

Hurricane Sandy caused severe flooding within the strong wind zone over the coastal areas of New York City and New Jersey (<https://www.weather.gov/okx/Hurricane>). The Battery was located at the outer edge of the strong wind zone on the north, while Atlantic City and Cape May were close to the center and on the left of Hurricane Sandy, respectively. The H- and NH-coupled models substantially improved the surge level prediction at the Battery but overestimated the surge level at Atlantic City and Cape May. Kang and Xia (2020) applied the uncoupled FVCOM to simulate the Sandy-induced storm surge over the Maryland coast, finding the model under-produced the water level at Atlantic City and

the Battery. It should be pointed out that the ocean model grid used in these experiments did not include the land territory required for coastal inundation. Taking storm-induced flooding into account, the overestimation at these two stations could be caused by missing the coastal inundation process within the maximum wind zone. If that was the case, the surge level was substantially underestimated by the uncoupled FVCOM. We also found that wind-induced onshore water transport mainly caused the simulated surge. The overestimation on the left side of Sandy could be possible due to the failure to capture the asymmetrical spatial wind distribution in WRF.

b) Surface currents, temperatures, and salinities.

The simulated surface currents were compared with the HFR array-derived currents over the continental shelf. The uncoupled and coupled FVCOMs reproduced the rapid intensification of surface currents over the shelf during the Sandy crossing. Its temporospatial distribution matched well with the HFR array-derived flow field. For example, at 16:00 on 29 Oct., all models captured the storm-induced southward shelf flow (Fig. 8). The coupled models predicted a stronger vortex than the uncoupled model, which could be seen in the vortex size and currents in the offshore area. The coupled FVCOMs predicted slightly stronger surface currents than the uncoupled FVCOMs.

Meanwhile, no matter whether or not coupling with WRF, the simulated currents were more intense in the FVCOM-NH cases than in the FVCOM-H cases. Over the period from 00:00 on 28 Oct. to 16:00 on 29 Oct., the mean errors of the coupled model case were 0.2 m/s (H and NH) in speed and 23.4° (H) and 25.4° (NH) on direction, with current vector RMSEs of 0.3 and 0.4 m/s for the H and NH cases, respectively (Table 5). The uncoupled FVCOM model showed similar performance in the current speed simulation but a large bias in the current direction (Table 5). The simulated surface currents in four cases differed mainly around the hurricane tracks due to the different wind forcing distributions. The mean direction errors produced by the coupled models were $\sim 5\text{--}7$ ° smaller, showing a 21.4% improvement. Considering the largest HFR measurement uncertainty of ~ 10.0 cm/s in the current speed and ~ 30 ° in the current direction (Sun et al., 2016), the coupled and uncoupled FVCOM models were robust to simulate the hurricane-induced surface flow over the shelf. Based on the comparison results, the coupled model was sufficient to simulate the storm-induced shelf flow. WRF + FVCOM-NH produced a more intense vortex over the shelf than WRF + FVCOM-H. Unfortunately, the HFR failed to obtain high-quality data when Sandy arrived over the shelf. We could not evaluate whether WRF + FVCOM-NH and WRF + FVCOM-H were more robust in resolving the storm-induced cyclonic flow than the uncoupled FVCOM.

We compared the simulated and observed temperatures and salinities in the ocean model domain for both uncoupled and coupled model cases. The observational data were from NODC, NODC, NERACOOS, and NEFSC, containing 61 stations and 12,961 records. Unfortunately, most of the T_s and S measurements were made outside Sandy's maximum wind zone. Without data assimilation, both uncoupled and coupled models provided a reasonable simulation of the water properties with RMSEs of 1.7° C in temperature and 0.6–0.7 PSU in salinity (Table 6).

4. Discussions

4.1. Atmospheric feedbacks

The WRF + FVCOM results showed that the ocean feedback to the atmosphere strengthened the hurricane's intensity by increasing the maximum wind velocity, reducing the radius of the max-wind zone, and causing a drop in the SLP minimum (Fig. 9). The highest wind speeds all occurred in the left-rear area of the hurricane center for the three cases. The maximum wind speed was 32.1 m/s for the uncoupled WRF case, 33.6 m/s for the WRF + FVCOM-NH case, and 34.2 m/s for the WRF + FVCOM-H case. Although the differences were only ~ 2.0 m/s, the

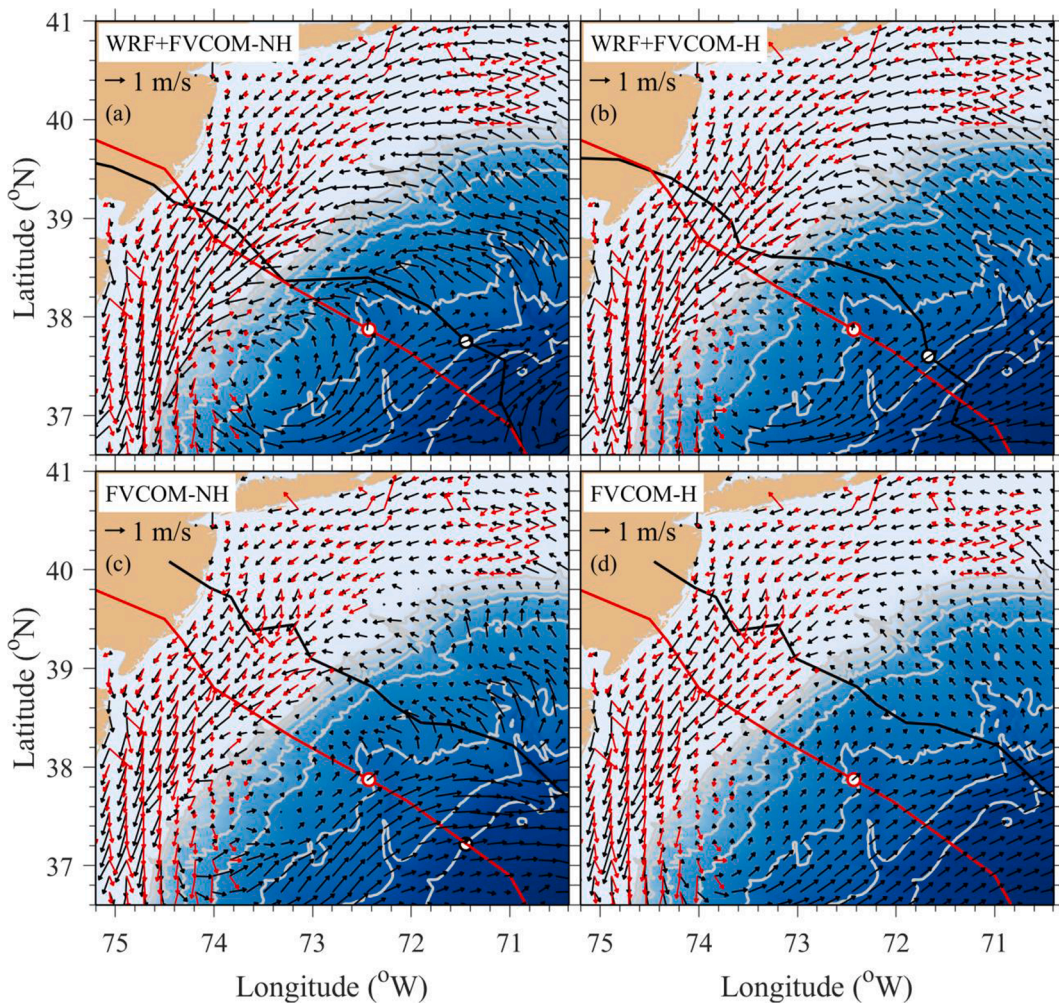


Fig. 8. Comparisons between the simulated and observed surface currents at 16:00 on 29 Oct. 2012 for the WRF + FVCOM-NH, WRF + FVCOM-H, FVCOM-NH, and FVCOM-H cases. In each panel, red arrow: observed surface currents; black arrow: simulated surface currents; red line: the historical center track; black line: the simulated tracks.

Table 6

RMSE between the observation and the simulated results of the WRF + FVCOM-NH, WRF + FVCOM-H, FVCOM-NH, and FVCOM-H cases on ocean temperature and salinity. RMSE_T: RMSE of ocean temperature; RMSE_S: RMSE of salinity.

Variables	WRF + FVCOM-NH	WRF + FVCOM-H	FVCOM-NH	FVCOM-H
RMSE _T (°C)	1.7	1.7	1.7	1.7
RMSE _S (PSU)	0.7	0.7	0.6	0.6

radius of the max-wind zone was about 1.5 smaller in the coupled cases with the inclusion of oceanic feedback from the ocean model (Fig. 9a, d, and g). The OceanSat-2 satellite images showed that the cyclonic wind vortex in Hurricane Sandy was strongly asymmetric and elliptically shaped, with its maximum on the left and rear areas of its center (Fig. 1). This feature was well captured by the coupled models but not by the uncoupled model. The coupled model also predicted the most intensive vorticity at the center, with a value of $2.1 \times 10^{-3} \text{ s}^{-1}$, 23.5% greater than those in the uncoupled WRF case (Fig. 9b, e, and h). It implied that the air-sea interaction process tended to reduce the storm size and lead to a vortex intensification. The maximum horizontal velocity shear zones, which occurred on the front and rear areas of the hurricane center, were mainly in the north-south orientation in the WRF + FVCOM-NH case, while in the northeast-southwest orientation in the WRF + FVCOM-H

case (Fig. 9b and e). It suggests that even under a lower-order approximation, the WRF + FVCOM-NH-predicted wind vortex could considerably differ from the WRF + FVCOM-H. The central SLPs were 988.1 hPa in the WRF + FVCOM-NH case (Fig. 9c), 988.3 hPa in the WRF + FVCOM-H case (Fig. 9f), and 989.8 hPa in the uncoupled WRF case (Fig. 9i). The slight decrease of the central SLP and intensification in the wind in the WRF + FVCOM-NH case could result in a more asymmetrically-distributed SLP field relative to the hurricane center (Fig. 9c).

Three transects across the hurricane were drawn to compare the cross-center distributions of the 10-m wind speed and SLP at the selected times for three cases (Fig. 10c). The storm center arrived at the slope at 21:00 on 29 Oct. for the two coupled cases and at 01:00 on 30 Oct. for the uncoupled case. The simulated wind was strongest on the left side than on the right side, with the sharpest gradient in the coupled case (Fig. 10a). At the selected times, the maximum wind speed in the coupled model cases reached $\sim 31.0 \text{ m/s}$, $\sim 4.0 \text{ m/s}$ stronger than the maximum wind speeds predicted on the left and right sides in the uncoupled WRF case. Compared with WRF + FVCOM-H, the WRF + FVCOM + NH-produced cross-hurricane wind shear was similar on the left side but more substantial on the right side. The coupled model-predicted minimum SLP errors were 0.2 for NH and -1.7 hPa for H, compared with 3.6 hPa for the uncoupled WRF case (Fig. 10b).

The simulated heat flux fields substantially differed between the uncoupled and coupled cases (Fig. 11). All three cases were selected

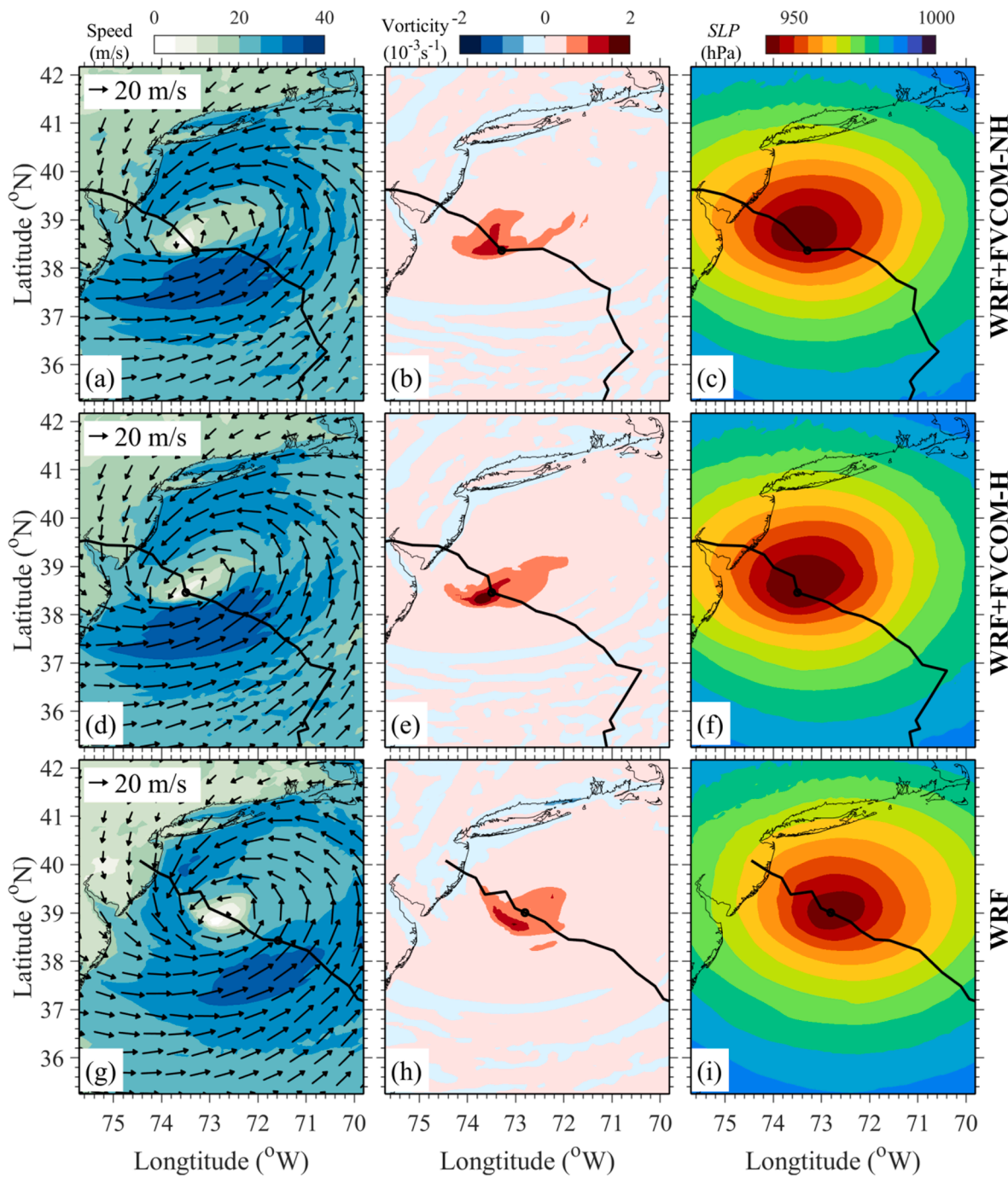


Fig. 9. Comparisons of the 10-m wind (the left column), 10-m wind vorticity (the middle column), and SLP (the right column). Snapshots were taken at 21:00 on 29 Oct. 2012 for the coupled cases and 01:00 on 30 Oct. 2012 for the uncoupled WRF case.

simultaneously at 21:00 on 29 Oct. In these three cases, the ocean lost and gained heat in the rear and front areas of the hurricane center, respectively. The heat loss from the ocean to the atmosphere was dominated by the latent heat flux. In the WRF + FVCOM-NH case, the maximum net heat loss in the left and rear area of the hurricane center was $-1,710.7 \text{ W/m}^2$, along with the latent heat flux of $-1,356.2 \text{ W/m}^2$ and the sensible heat flux of -431.6 W/m^2 (Fig. 11a-c). In the front and right area of the hurricane center, the maximum net, sensible and latent heat gains were 734.4, 261.5, and 411.4 W/m^2 , respectively. WRF + FVCOM-H predicted similar patterns of the net, latent and sensible heat fluxes as WRF + FVCOM-NH. The difference was in the heat content. Considering the mean heat fluxes averaged over the max-wind zone within 150 km, the difference in the heat flux was substantial between

the two cases. The net, latent, and sensible heat fluxes through the air-sea interface were -449.4 , -341.6 , and -111.9 W/m^2 in the WRF + FVCOM-NH case (Fig. 11a-c) and -471.5 , -386.2 , and -128.3 W/m^2 in the WRF + FVCOM-H (Fig. 11d-f). It indicated that the accumulated heat content loss within the max-wind zone predicted by the H-coupled model was larger than that predicted by the NH-coupled model, with differences of 4.9%, 13.0%, and 14.7% in the net, latent, and sensible heat fluxes, respectively. The major difference was in the latent heat flux loss areas. WRF + FVCOM-H predicted a larger area for the latent flux loss, while this area shrank towards the hurricane center in the WRF + FVCOM-NH case.

The uncoupled WRF also predicted the same intense latent flux loss in the rear area of the hurricane. However, the location was 200–300 km

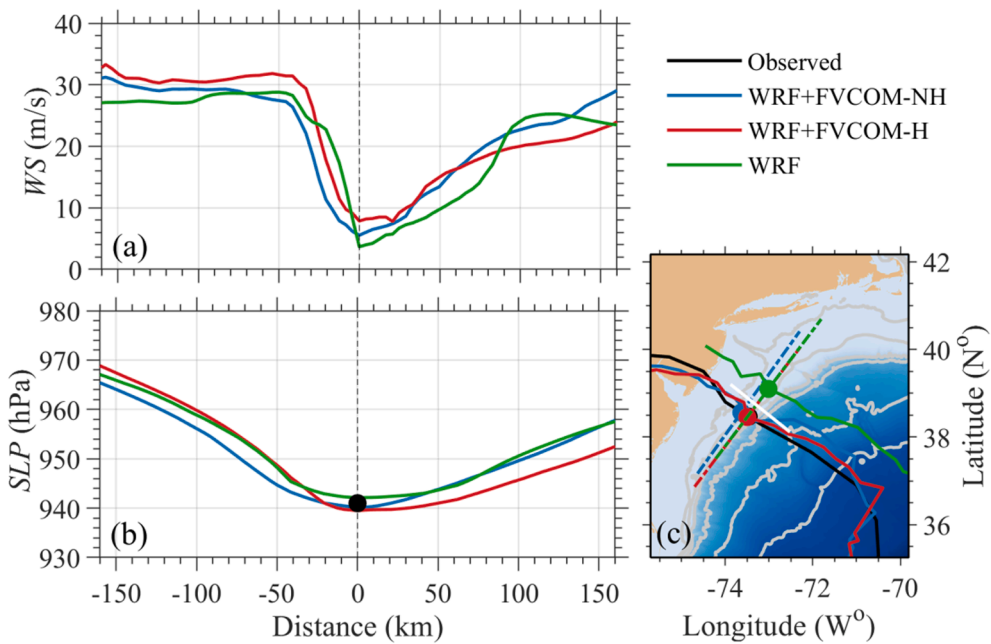


Fig. 10. Comparisons of the 10-m wind speed (a) and SLP (b) on the selected sections across the hurricane center (a) for the WRF + FVCOM-NH, WRF + FVCOM-H, and uncoupled WRF cases. Snapshots were taken at 21:00 on 29 Oct. 2012 for the coupled cases and 01:00 on 30 Oct. 2012 for the WRF cases. The black point in (b) is observed SLP at the storm center. The white line in (c) is the transect used in Fig. 15.

away from the hurricane center (Fig. 11g-i). The latent flux played a critical role in supplying heat energy to the hurricane. The uncoupled WRF underestimated the oceanic heat energy transfer around the hurricane center. It explained why the WRF underestimated the hurricane's intensity and caused a considerable bias in its moving path. The coupled model-predicted distribution of the maximum latent heat flux loss in the left and rear areas of the hurricane center was consistent with the OceanSat-2 satellite-derived surface wind distribution of Hurricane Sandy. The hurricane gained significant energy from the enhanced latent heat flux in the left and rear areas and lost the latent heat flux in the front and right regions, leading to an asymmetric wind field with a maximum on the left side.

Due to the lack of temperature data over the shelf, we cannot simply conclude which model provided the more realistic heat fluxes. Based on the comparison results with the observed SLP at the hurricane center, the NH process played a specific role in improving the SLP simulation before the hurricane made landfall. Since the accumulated heat contents within the max-wind zone were in order of the difference between the two cases, a further investigation of the storm-induced heat exchanges between the hurricane and the ocean should be paid attention to in storm monitoring in the future.

The air potential temperatures and water vapor ratios were compared along Section S1 (see Fig. 5a) in the deep ocean (Fig. 12). Different times were selected for the three cases when their hurricane centers arrived at S1. The three instances shared similar patterns in the distribution of temperature. The air potential temperatures were lower at the sea surface and increased with height. The coupled models predicted an air potential temperature minimum at a left-side location of ~ 2 km away from the hurricane center. This coldest area also appeared in the uncoupled model case, but the place was left-shifted ~ 0.5 km. For all uncoupled and coupled cases, the model-simulated water vapor ratios were highest at the sea surface, with a maximum at the hurricane center. The difference was in magnitude. The air-sea coupling produced more water vapors, with a ratio of about 4.6% higher than the uncoupled case. The difference implied that storm-induced air-sea interaction could enhance the oceanic energy loss via the latent heat flux. Meanwhile, the storm's vortex intensification and size reduction agreed well with the water vapor distribution. The maximum gradient of the water

vapor ratio appeared around an isoline of 16×10^{-3} . Taking this isoline as the boundary of the most considerable latent heat flux, we calculated the radius of the significant water vapor ratio area. It showed a range of ~ 300 km in the coupled model cases, which was about 30 km smaller than the uncoupled case.

4.2. Oceanic responses

a) Horizontal currents, SST, and MLD.

The hurricane-induced high winds created a rapidly-varying strong current over the continental shelf. This current was much stronger in the coupled cases than in the uncoupled cases (Fig. 13a, d, g, and j). If comparing the simulated surface currents at the closest locations of storm centers, the uncoupled FVCOM model could also produce a similar shelf flow. However, the intensity of this flow was less than 0.6 m/s over the shelf, even though the RMSEs during the period with available measurements were in the same order of magnitude for the coupled and uncoupled cases. This difference was related to the time scale of wind forcing. In the uncoupled cases, the ocean model was driven by hourly wind forcing output from the uncoupled WRF case. The wind intensity was weaker in these cases (Fig. 9), and it did not resolve the rapid wind variation within an hour. The stronger currents predicted by the coupled models agreed with the wind-induced vortex intensification resulting from the air-sea interaction (Fig. 13a, d). The intensified cyclonic currents directly enhanced the surge prediction along the coast and thus coastal inundation. WRF + FVCOM-NH predicted stronger near-surface currents than WRF + FVCOM-H. In fact, the major difference between these two cases was in the rear area of the hurricane center (Fig. 13a and d), where the maximum current speed difference could be up to ~ 0.2 m/s. It implied that WRF + FVCOM-NH tended to intensify the hurricane-induced vorticity in the ocean.

The ocean model used for either coupling or no-coupling included the Gulf Stream. The Gulf Stream flowed into the ocean model domain on the southern boundary and flowed out of the ocean model domain on the open ocean boundary on the east. When the hurricane arrived over the slope, it created a strong cyclonic-rotating flow near the sea surface. A robust offshore flow, in order of up to ~ 2.0 m/s, occurred near the sea

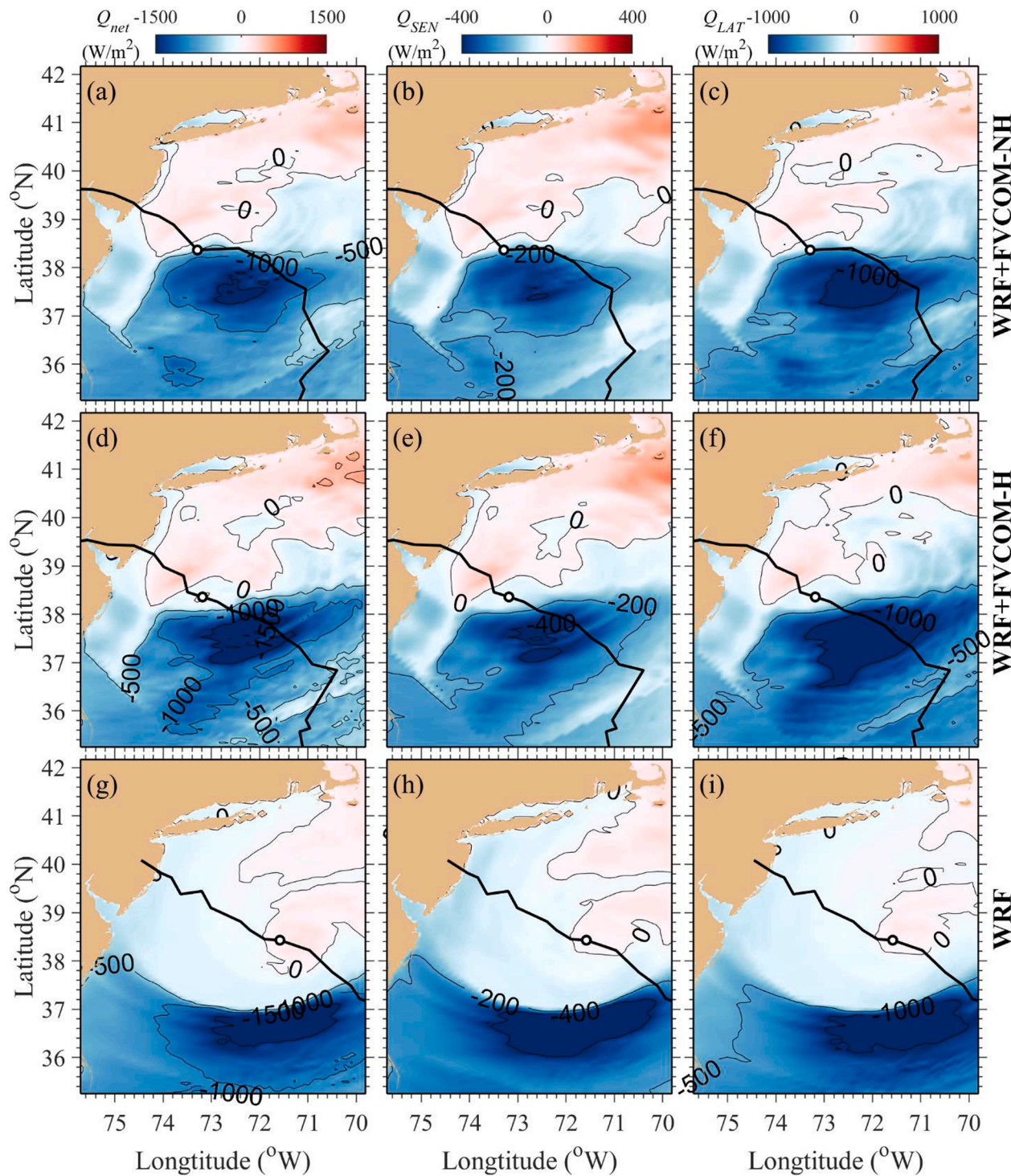


Fig. 11. Comparisons of net heat flux (the left column), sensible heat flux (the middle column), and latent heat flux (the right column) at 21:00 on 29 Oct. 2012 for the WRF + FVCOM-NH, WRF + FVCOM-H, and uncoupled WRF cases. Negative values mean the ocean loses energy.

surface in the Gulf Stream area, which substantially changed the near-surface current over there. The storm disturbance rapidly dispersed. The Gulf Stream's surface flow returned to a normal condition a few hours after the hurricane passed.

The simulated SST and MLD fields were compared among the four cases (Fig. 13b, e, h, and k). The SST in the frontal area of the hurricane center was similar, with a value under 18 °C on the continental shelf. In the rear area of the hurricane center, the SSTs were higher in the coupled cases than those in the uncoupled cases. In the coupled model cases, the SST in the southern area of the domain was mainly above 26 °C (Fig. 13b

and e). The 26 °C isoline retreated offshore in the uncoupled FVCOM cases (Fig. 13h and k). As pointed out by Emanuel (2003), the hurricane acts like a Carnot heat engine system. In this system, although the SST differences between the coupled and uncoupled cases were slight, such a little air-sea temperature difference could substantially change the kinetic energy in a storm. That was demonstrated in the WRF + FVCOM simulation in this work.

The NH dynamics led to a significant change in SST. WRF + FVCOM-NH predicted an essentially different SST field compared with WRF + FVCOM-H. In the WRF + FVCOM-H case, the southern region in the

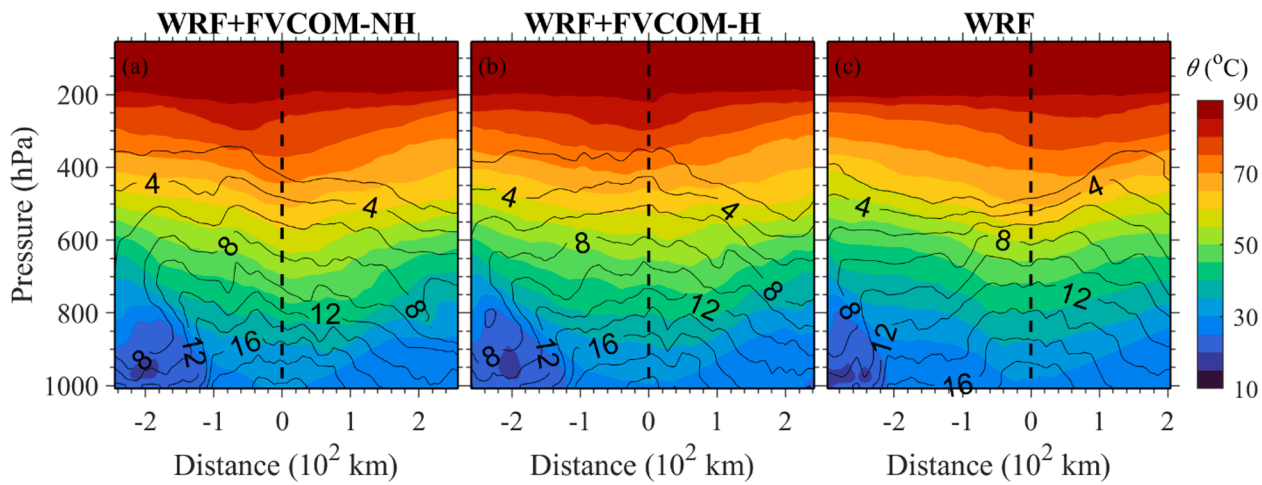


Fig. 12. Distributions of the air potential temperature and water vapor ratio on S1. The black lines are the isolines of the water vapor ratio (unit: 10^{-3}). The colors show the air potential temperature. Snapshots were taken at 15:00 on 29 Oct. 2012 for the coupled cases and 19:00 on 29 Oct. 2012 for the uncoupled case.

ocean domain, in the rear of the hurricane center, was dominated by warm water with a temperature of 26°C (Fig. 13e). This feature remained little changed during the hurricane crossing period. In the WRF + FVCOM-NH case, the SST remarkably dropped in the rear area of the hurricane center, especially underneath the max-wind zone of the hurricane (Fig. 13a). Except in the left front area of the hurricane center, the SST was lower in the WRF-FVCOM-NH case than in the WRF-FVCOM-H case. The maximum SST difference between these two model cases was up to $\sim 2.0^{\circ}\text{C}$. The most substantial difference was on the right side of the hurricane center and over the slope.

Correspondingly, the MLDs were shallower in the coupled cases than those in the uncoupled cases (Fig. 13c, f, i, and l). Before the hurricane arrived over the shelf, the simulated MLD was ~ 40 m in the inner-shelf region. As the hurricane came, the coupled and uncoupled FVCOMs showed that the MLD was deepened on the right side of the hurricane center and became shallower on the left side of the hurricane center. Although the wind was stronger in the coupled cases, the simulated MLD was shallower in the coupled cases than in the uncoupled cases, especially on the left side of the hurricane center.

The MLDs predicted by WRF + FVCOM-NH and WRF + FVCOM-H showed a minor difference over the continental shelf and along the coast, but they were distinct in the deep region off the slope (Fig. 13c and f). Taking the hurricane trajectory as a reference point, WRF + FVCOM-NH predicted a deeper MLD on the right side and a shallower MLD on the left side. The maximum difference could be up to ~ 20 m. This result agreed with the distribution of vertical velocity difference between the NH and H cases, which showed that WRF + FVCOM-NH produced a strong vertical velocity on the right side.

b) Vertical velocities.

In general, the vertical velocity predicted with the NH dynamics was much stronger than that with the H dynamics, no matter whether WRF and FVCOM were coupled. (Fig. 14a-f). Although they were 10^{-4} m/s, the vertical velocity predicted by WRF + FVCOM-NH was about 2–3 times larger. The colder SST areas matched well with the more substantial vertical velocity difference areas. The 2-km resolution grid could not fully resolve the NH convection process over the continental shelf. This feature was evident in Fig. 14a-c, which showed a minor difference in the vertical velocity in the shelf region between the NH- and H-coupled models. The larger vertical velocity difference found in the deep ocean off the slope suggests that as the lower-order approximation, the NH process-induced vertical velocity could enhance surface cooling within the storm-influenced area.

A transect along the hurricane track was selected to compare

temperature and vertical velocity (Fig. 15). For all four cases, the shelf was well mixed from the surface to the bottom, with a temperature of $\sim 17^{\circ}\text{C}$, and strongly stratified in the open ocean off the slope. Near the hurricane center, the MLD was sharply decreased due to the weak wind. On the rear of the hurricane center, the MLD was gradually deepened from 28 m to 78 m. For the cases without the air-sea coupling, the temperature was 1–2 °C lower in the upper ocean in the open ocean. The MLD in this case was 3–12 m deeper than the MLD in the coupled model.

The substantial difference was at the shelf break. WRF + FVCOM-NH predicted a strong upwelling over the slope, advecting the 14° cold water upward (Fig. 15a-b). This upwelling was also viewable in the WRF + FVCOM-H case, but the magnitude is one to two times weaker (Fig. 15e-f). A relatively strong downwelling was also found off the slope, pushing the warm water downward. This downwelling did not exist in the WRF + FVCOM-H case. In both coupled cases, storm-induced vertical mixing mainly occurred in the upper 50-m layer, while the WRF + FVCOM-NH predicted a deeper MLD in the deep region off the slope. This difference matched the vertical velocity difference, suggesting that the NH process-induced vertical convection, even under a lower-order approximation, could enhance vertical mixing in the open ocean.

c) Surge levels.

The storm-induced surge level was related to the wind direction, storm translation direction and speed, and the radius of maximum winds (Beardsley et al., 2013; Chen and Qin, 1985a, b; Weisberg and Zheng, 2006a, b, 2008; Rego and Li, 2009; Chen et al., 2013a; Kang and Xia, 2020). For the coupled cases, the water elevations at the coast of New Jersey and Long Island were higher than 1.5 m, with a maximum of 2.2 m (Fig. 16a, c). For the uncoupled cases, the model-predicted water elevation around this coast was around 1 m, with a maximum of 1.9 m (Fig. 16b, d). The distributions of the maximum elevation also primarily differed in these two cases. The maximum elevation mainly occurred along the New Jersey coast in the coupled model case, but it was relatively uniformly distributed along the Long Island and New Jersey shore in the uncoupled cases. The differences were due to the distinct radius of the max-wind zones predicted by WRF + FVCOM and WRF. WRF + FVCOM produced a smaller max-wind zone radius and much stronger wind in this zone.

WRF + FVCOM-NH did not change the temporospatial distribution of the water elevation along the coast during Hurricane Sandy's crossing (Fig. 16a-b). The WRF + FVCOM-NH predicted a slightly high surge level, about 0.1 m higher than the WRF + FVCOM-H case. Because of it, the 1.0-m water elevation contour, which was bounded at the eastern tip of Long Island in the hydrostatic coupled model case, extended

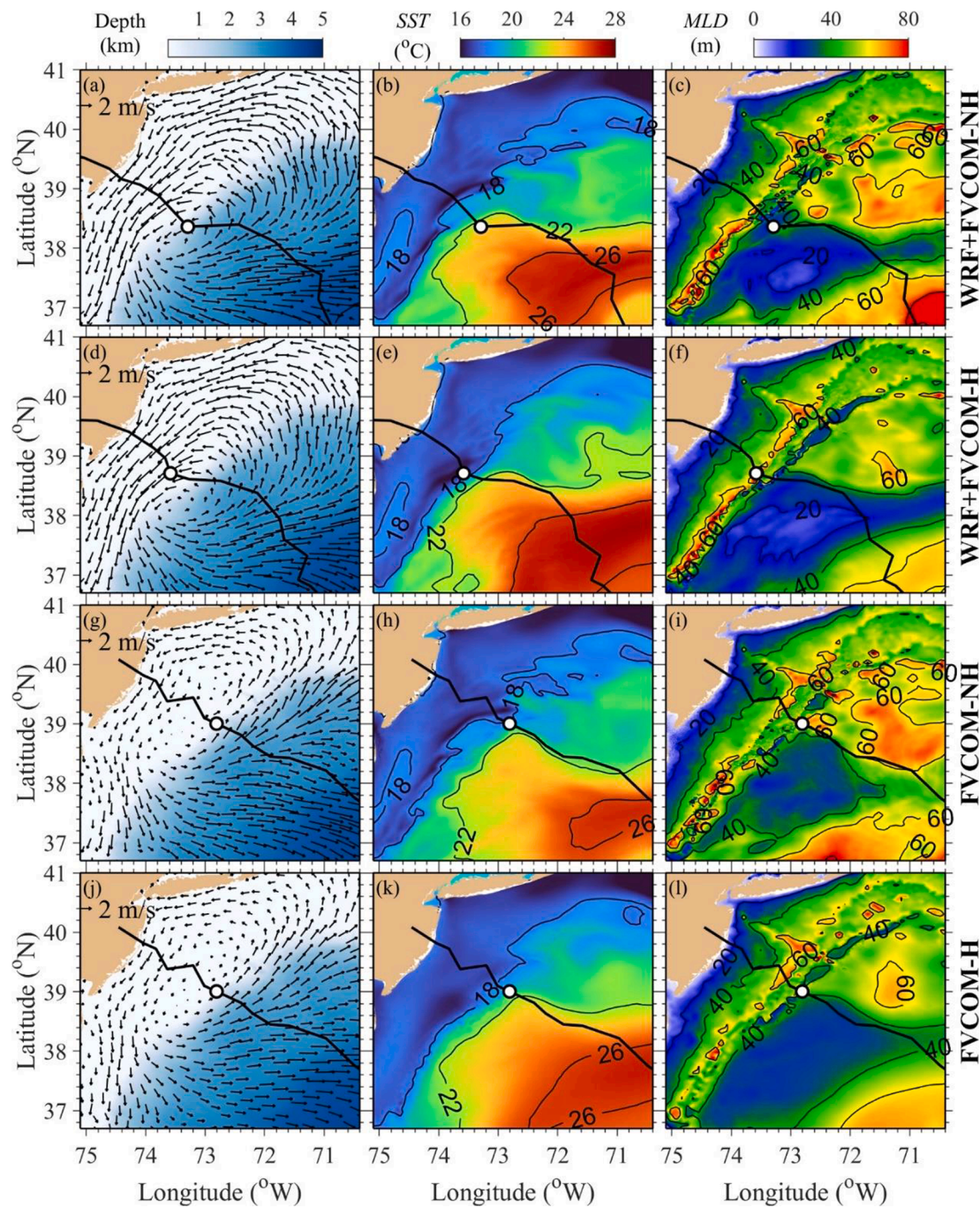


Fig. 13. Comparisons of surface currents (the left column), SST (the middle column), and MLD (the right column) for the WRF + FVCOM-NH, WRF + FVCOM-H, FVCOM-NH, and FVCOM-H cases. Snapshots were taken at 21:00 on 29 Oct. 2012 for the coupled cases and 01:00 on 30 Oct. 2012 for the uncoupled cases.

northward to Narragansett Bay coast, RI.

The water transport entering the area from the selected boundary is shown in Fig. 16e. The coastal surge was mainly caused by northeastward wind-induced onshore water transport. Both WRF + FVCOM-NH and WRF + FVCOM-H showed that the total transport rapidly increased as the hurricane approached the coast and reached its maximum at 02:00 on 30 Oct. After the hurricane made landfall, it quickly decreased. WRF + FVCOM-NH produced a slightly higher maximum transport at a time than WRF + FVCOM-H but lower total transport over 3 days. Over three days, the total transport was 29.9 Sv for the WRF + FVCOM-NH case and 30.0 Sv for the WRF + FVCOM-H case. The uncoupled FVCOM-NH also predicted the same spatial distribution of the water elevation as the coupled models. However, the

simulated water elevation and the transport were remarkably lower than in the coupled model cases (Fig. 16b). Over the three days, the total onshore transport was 22.3 Sv, $\sim 25.7\%$ less than the WRF + FVCOM-H case and $\sim 25.4\%$ less than the WRF + FVCOM-NH case.

d) Inertial resonances.

Price (1981) examined the oceanic response to an idealized tropical storm. He found that when a storm passes a location, the wind rotates clockwise on the right and anticlockwise on the left side. When the clockwise rotation is close to the inertial period, it could cause strong inertial currents in the upper OML, producing an intense cold wake on the right side. Following his findings, we quantitatively derived the

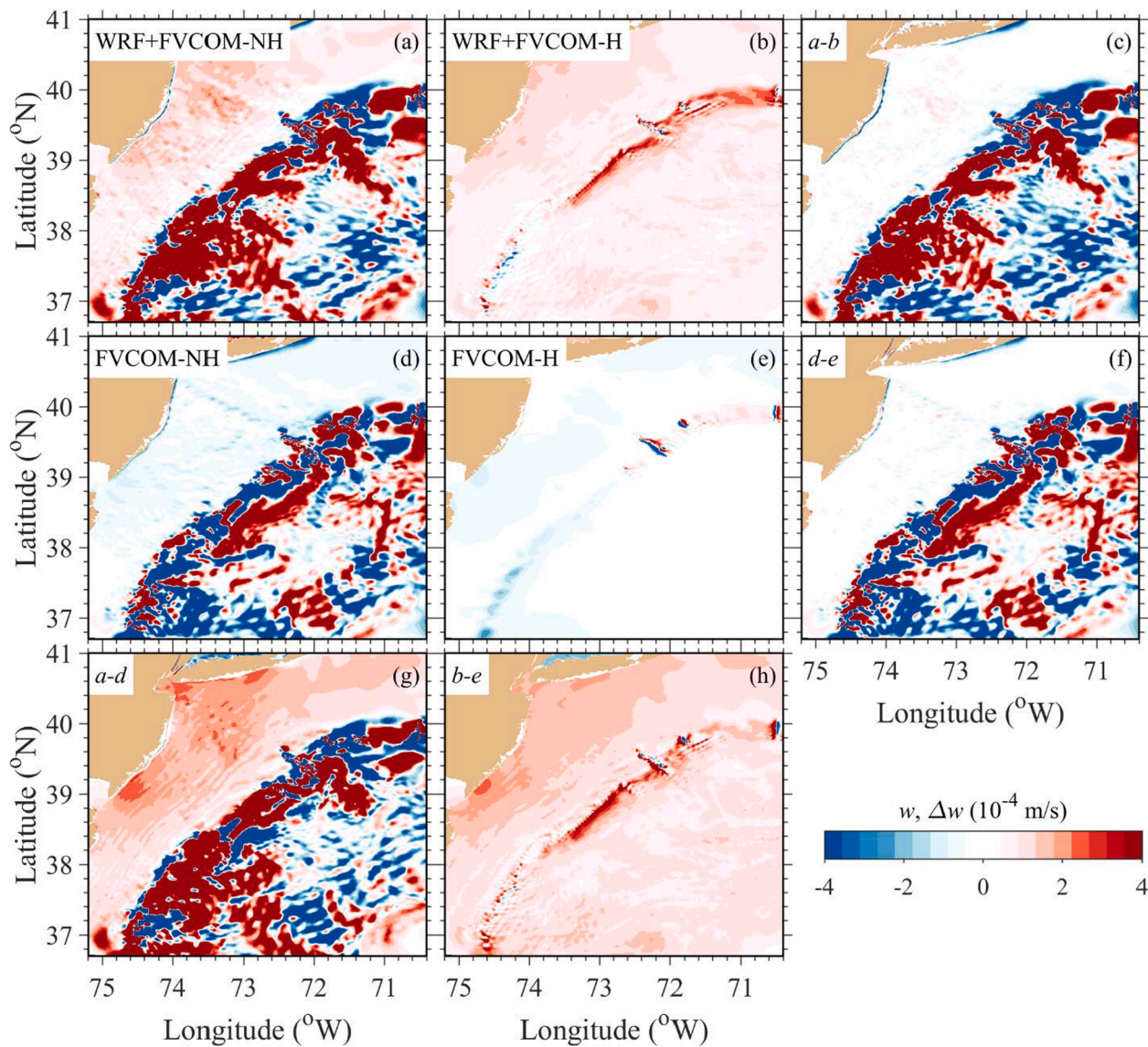


Fig. 14. The surface vertical velocity (w) and their differences (Δw) for the WRF + FVCOM-NH, WRF + FVCOM-H, FVCOM-NH, and FVCOM-H cases. Snapshots were taken at 21:00 on 29 Oct. 2012 for the coupled cases and 01:00 on 30 Oct. 2012 for the uncoupled cases.

equation capable of determining the location where the maximum oceanic response could occur. It is given as.

$$R = \gamma U_H \quad (1)$$

where $\gamma = \frac{\theta}{f\alpha}$, U_H is the storm translation speed (unit: m/s), R is the radius from the storm center where the inertial resonance occurs (unit: km), θ is the rotating angle of the storm center relative to the R -location, f is the local inertial frequency, and $\alpha = \tan\theta$. The detail is given in Appendix B.

Price (1981) analyzed six tropical storm data, including Clara (1955), Wanda (1956), Shirley (1965), Ella (1968), Tess (1975), and Eloise (1975). He reported that the strong U_H (>6 m/s) provided a favorable condition for inertial resonance responses on the right side of the storm center. Hurricane Sandy's center path was around $\sim 37^\circ\text{N}$, and γ was ~ 9.48 . As Sandy entered the FVCOM domain, the observed U_H increased from ~ 6.0 m/s to ~ 9.0 m/s and reached its maximum of 11 m/s (Fig. 17a). It made its landfall at U_H of ~ 8.0 m/s. The WRF + FVCOM-NH and WRF + FVCOM-H reasonably captured the observed U_H , while the uncoupled WRF significantly underestimated U_H , especially over the period before the storm entered the continental shelf

(Fig. 17a). The WRF + FVCOM-NH captured the U_H maximum and its timing better than the other two cases. As a result, R calculated based on the simulated U_H was close to the linear U_H - R line derived by Eq. (1) for the coupled models, but it was far away for the uncoupled model (Fig. 17b). The radii of the maximum oceanic responses were ~ 100 , 120, and 65 km for the WRF + FVCOM-NH, WRF + FVCOM-H, and uncoupled WRF cases, respectively (Fig. 17b). There were two reasons for the smaller radius in the uncoupled case: 1) the lower transition speed; 2) the mismatch between the radius and the transition speed due to the uncoupled process. Two transects (named S1 and S2 in Fig. 5a) were selected to examine the oceanic response to Sandy. S1 was located in the open ocean, with depths varying around 3000–4000 m. S2 was located on the shelf break, with a depth of around 500–1500 m. Both transects are across the hurricane track, with a total breadth of ~ 500 km. Based on the IBTrACS observational data, Sandy arrived at S1 at around 1300 29 Oct. and then at S2 5 h later. Using the WRF + FVCOM-H, for example, we examined the changes in the wind direction and frequency at the radius of 120 km during Sandy's crossing through S1 and S2 (Fig. 18). On the right side of the storm center, the wind rotated clockwise, and the rotating frequency was roughly equal to the Coriolis frequency when the storm center was near the transects (Fig. 18b, d).

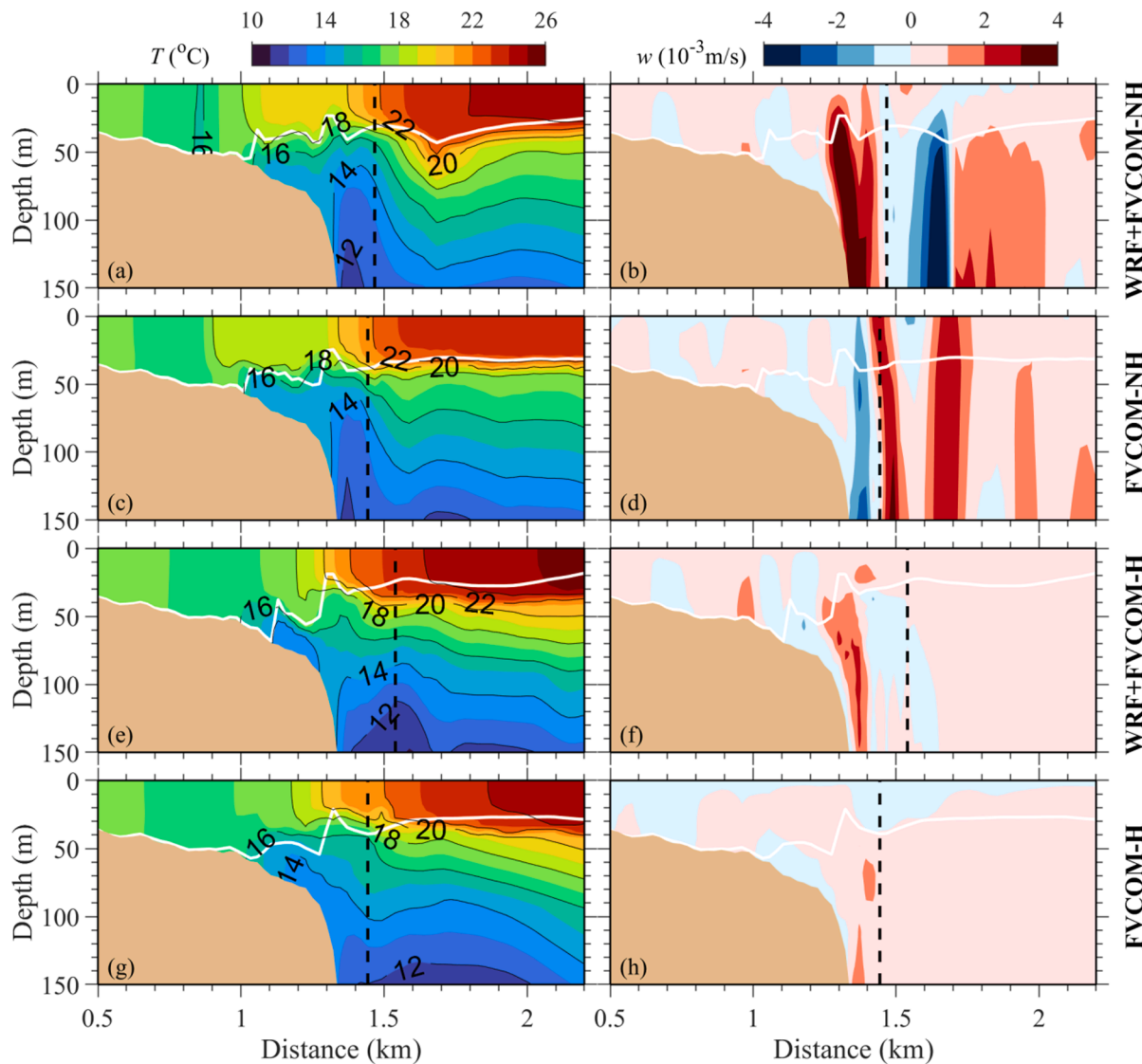


Fig. 15. Comparisons of simulated sea temperatures (left column) and vertical velocities (right column) on the selected section across the hurricane center (see Fig. 10a). Snapshots were taken at 21:00 on 29 Oct. 2012 for the coupled cases and 01:00 on 30 Oct. 2012 for the uncoupled cases. The white lines are the MLD.

They happened between 14:00–18:00 on 29 Oct. on S1 and 19:00–23:00 on 29 Oct. on S2. On these two transects, the near-resonance period lasted for ~ 4 h. On the left side, the wind rotated counterclockwise as the hurricane approached, and hence the wind rotating frequency was much lower than the Coriolis frequency (Fig. 18a, c). Also, the counterclockwise rotating wind produces positive vorticity, which cancels the clockwise-rotating inertial current energy so that no inertial resonance could occur (Kundu, 1986; Chen et al., 1996). The changes in wind rotating frequency in the WRF + FVCOM-NH and uncoupled WRF cases exhibited the same features as WRF + FVCOM-H, except that inertial resonance occurred at different locations and times.

The change of SST and ΔSST with time are examined on S1 and S2 during 28–31 Oct. for four model cases, including WRF + FVCOM-NH, WRF + FVCOM-H, FVCOM-NH, and FVCOM-H. FVCOM-NH and FVCOM-H were driven by the uncoupled WRF so that they had the same R for inertial resonance. ΔSST is defined as the SST difference relative to the initial SST at 00:00 on 28 Oct (Fig. 19). On S1, the SST varied substantially along the transect on the right side of the hurricane (Fig. 19a–d). For the WRF + FVCOM-NH case, the area over 0–100 km featured warm water, and the region of > 100 km featured cold water, resulting in a strong SST front at the warm-cold water transition zone. These features remained similar for the WRF + FVCOM-H, FVCOM-NH, and

FVCOM-H cases, except that the warm-cold water boundary shifted to 120 km in the WRF + FVCOM-H case and 65 km in the FVCOM-NH and FVCOM-H cases. The simulation results showed different hurricane paths and wind/SST distributions for the coupled and uncoupled cases.

To compare these two cases, we defined the x -axis as the distance relative to the simulated hurricane center. The substantial responses were evident in the SST frontal zone on the right sides for both coupled and uncoupled model cases. The maximum responses occurred during the near-resonance inertial period when the hurricane arrived. The responses were slightly stronger for the coupled model cases than for the uncoupled model cases, with a maximum SST change of $\sim 3.5\text{--}3.7$ °C, respectively (Fig. 19e–h). Including the NH process, no matter whether coupling with WRF, produced an intense SST front within the warm-cold water transition zone. Meanwhile, WRF + FVCOM-NH predicted a significant SST drop in an area 50 km away from the hurricane center on the right side after the hurricane crossing. This feature was also evident in an area 100.0 km away from the hurricane center in the WRF + FVCOM-H results, but the SST drop was much less. Similar features were also observed in uncoupled FVCOM-NH and FVCOM-H. FVCOM-NH produced a sharp SST drop of ~ 4.9 °C near the hurricane center, but this feature did not appear in FVCOM-H. Also, a second ΔSST peak occurred at 15:00 on 30 Oct. after the hurricane made landfall in the coupled

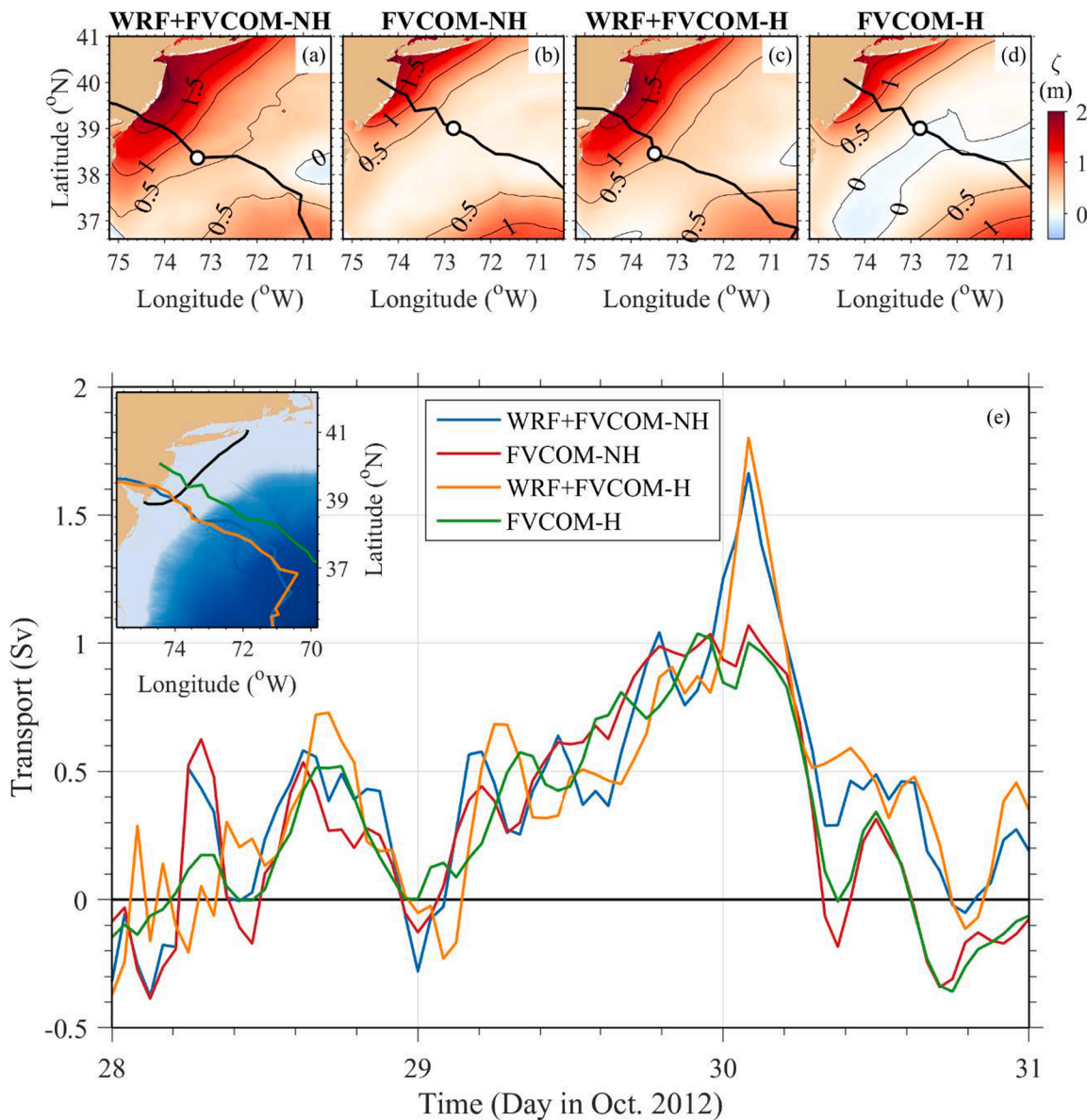


Fig. 16. Comparisons of the surface elevation ζ (a-d) and the onshore water transport (e) across the selected boundary (shown as the black line in the upper-left panel of (e) for the WRF + FVCOM-NH, WRF + FVCOM-H, FVCOM-NH, and FVCOM-H cases. Snapshots of (a-d) were taken at 21:00 on 29 Oct. 2012 for the coupled cases and 01:00 on 30 Oct. 2012 for the uncoupled cases.

model cases, more evident in the NH case. The maximum response areas shown in Fig. 19e-h were around 50–140 km, with a sharp gradient at ~ 100.0 km for WRF + FVCOM-NH, about 120–170 km, with a maximum at ~ 122 km for WRF + FVCOM-H, around 0–100 km with a sharp gradient at 65 km for FVCOM-NH, and approximately 40–80 km, with a maximum at ~ 65 km for FVCOM-H. Considering the simulated hurricane was not a perfect circular cyclone, the difference at the maximum response locations predicted by Eq. (1) and coupled/uncoupled models was reasonable.

Transect S1 was located in the deep ocean, where the turbulence dissipation was weak. The maximum responses shown in Fig. 19 were oscillations forced by inertial winds. The energies of these oscillations could remain relatively long due to weak dissipation. The oscillation energies were eventually dispersed by the barotropic and baroclinic gravity-inertial waves in the horizontal and vertical directions (Price, 1983; Chen and Qin, 1985c). These features were observed during tropical storms over the slope of the South China Sea by Li et al. (2021), showing that the lifetime of the oscillation could last for a week or even longer.

On S2, the warm-cold water boundary shifted toward the hurricane center, at ~ 40 km in the WRF + FVCOM-NH case, ~ 60 km in the WRF + FVCOM-H, and ~ 0 km in the uncoupled cases (Fig. 20a-d). Meanwhile, the SST varied considerably along the transect on the right side for all the simulation cases. The SST responses to inertial resonance were not apparent like that observed on S1. The substantial change in SST was evident on the left side, which was driven by other physical mechanisms. Looking at the right side, a 2.0°C sharp ΔSST change area appeared at 140–160 km and 160–180 km in the coupled and uncoupled NH cases, respectively (Fig. 20e, f). On the left and right sides of this narrow area, the SST was dropped by $\sim 2.0^{\circ}\text{C}$ after the storm translation speed reached local inertial frequency. The maximum response occurred at 19:00 on 29 Oct., consistent with the estimated near-resonance time. The coupled and uncoupled H models also predicted a considerable change in SST around the predicted location for inertial resonance on the right side after the storm translation speed reached the local inertial frequency. However, since the ΔSST change in that area were in the same order of magnitude as the surrounding areas, the resonance responses were not distinctly evident. In addition, the storm-induced SST

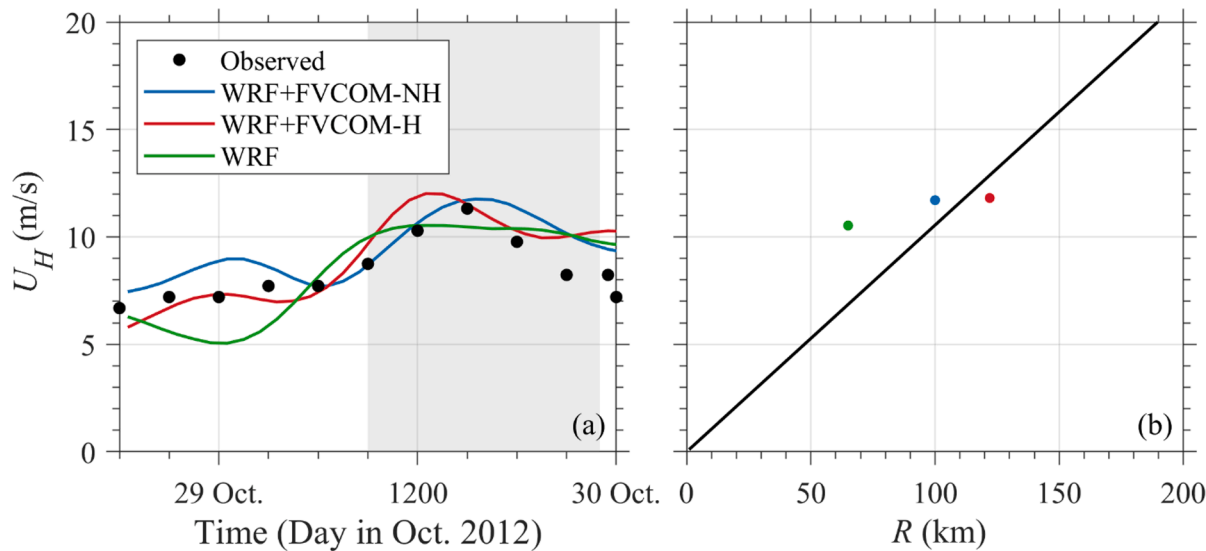


Fig. 17. The comparison of the storm translation speeds (a) and the relationship between the locations with the maximum oceanic responses and hurricane translation speeds (b). In (a), the shaded area shows the period that the storm moved in the fvCOM domain; U_H : the hurricane translation speed. In (b), R : the radius of the location with the maximum oceanic responses; the black line: the relationship line derived from Eq. (1) at the latitude of 37°N.

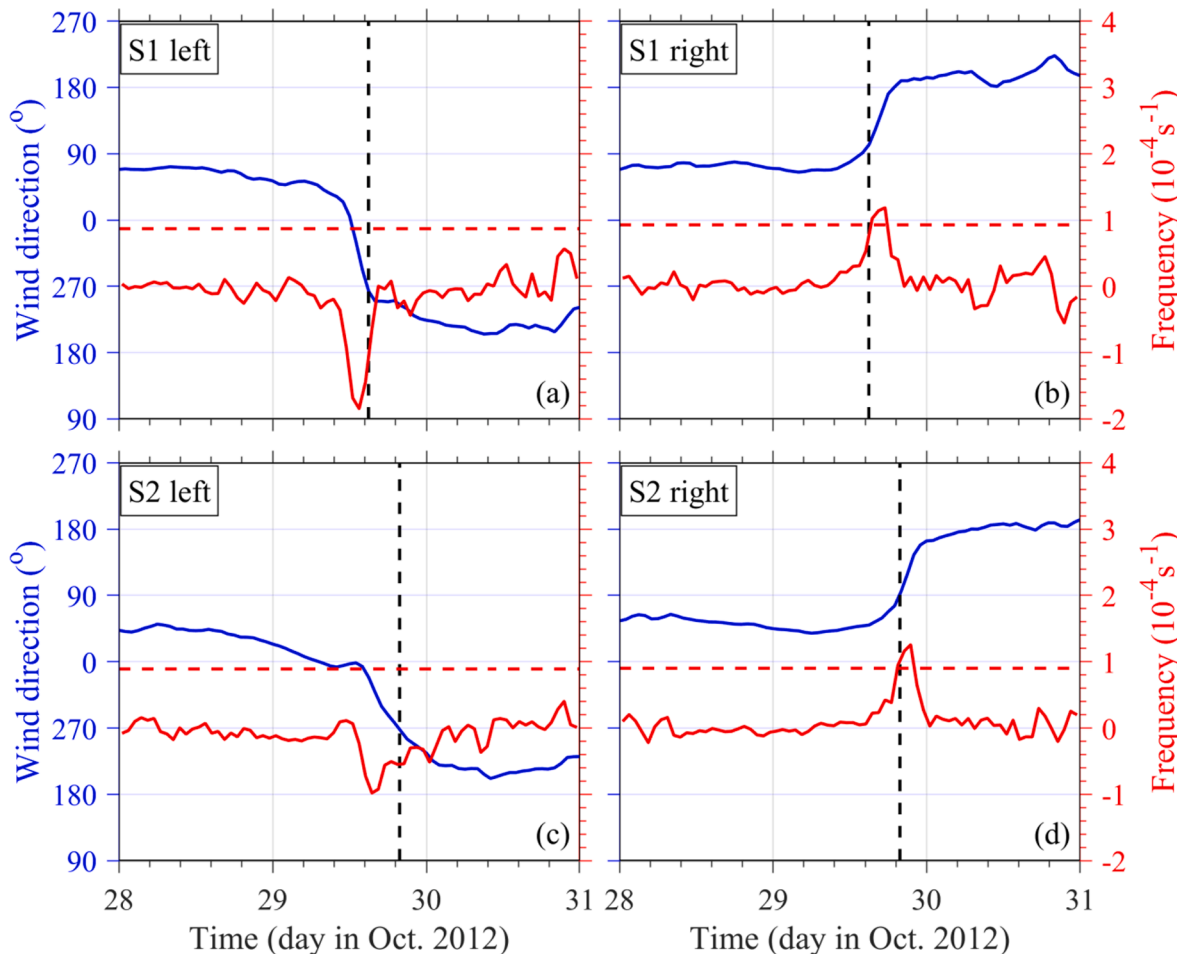


Fig. 18. The changes of the wind direction and rotating frequency with time at two points on both left and right sides of the storm center on S1 (a-b) and S2 (c-d) for the WRF + fvCOM-H case. Blue solid lines: wind direction; solid red lines: wind rotation frequency; red dashed lines: Coriolis frequency; black dashed lines: the time hurricane arrived at the transects.

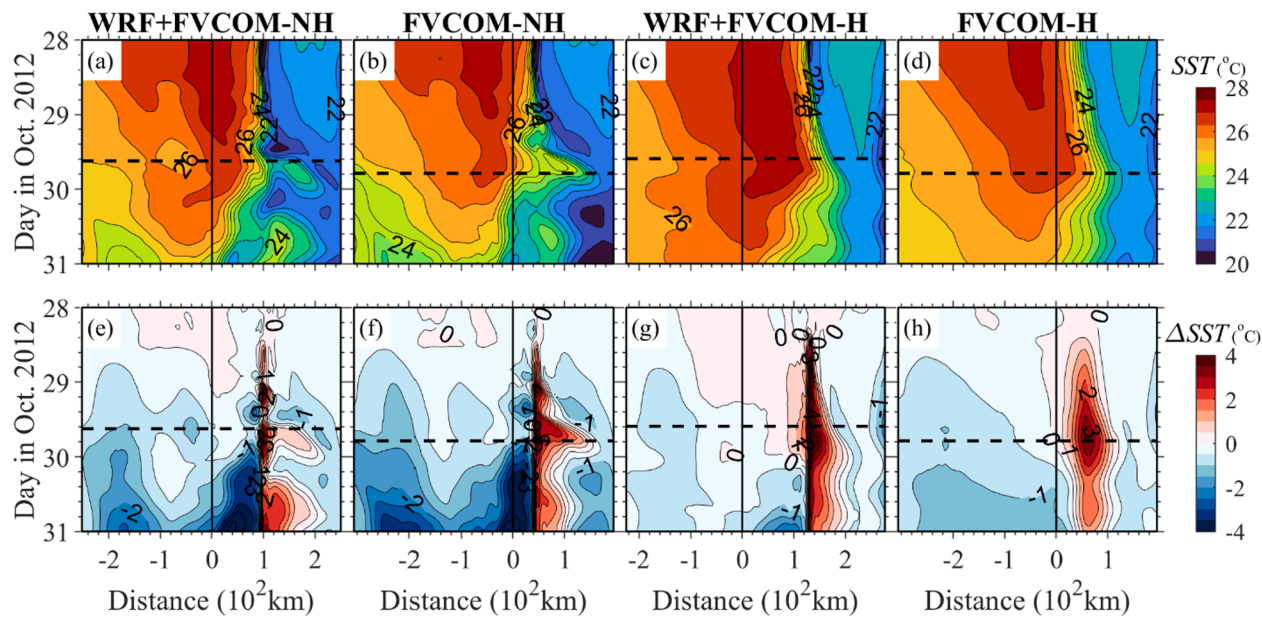


Fig. 19. The SST (a-d) and ΔSST (e-h) changes with time at S1 for the WRF + FVCOM-NH, FVCOM-NH, WRF + FVCOM-H, and FVCOM-H cases. ΔSST is the SST difference relative to the initial SST at 00:00 on 28 Oct. 2012. The y-axis is the time, and the x-axis is the distance relative to the hurricane center. Positive (negative) x: right (left) of the storm center. Black dashed lines: the time at which hurricane arrived at the transects; black solid lines: the origin of the x-axis, defined as the location of the hurricane center when the maximum inertial response is reached.

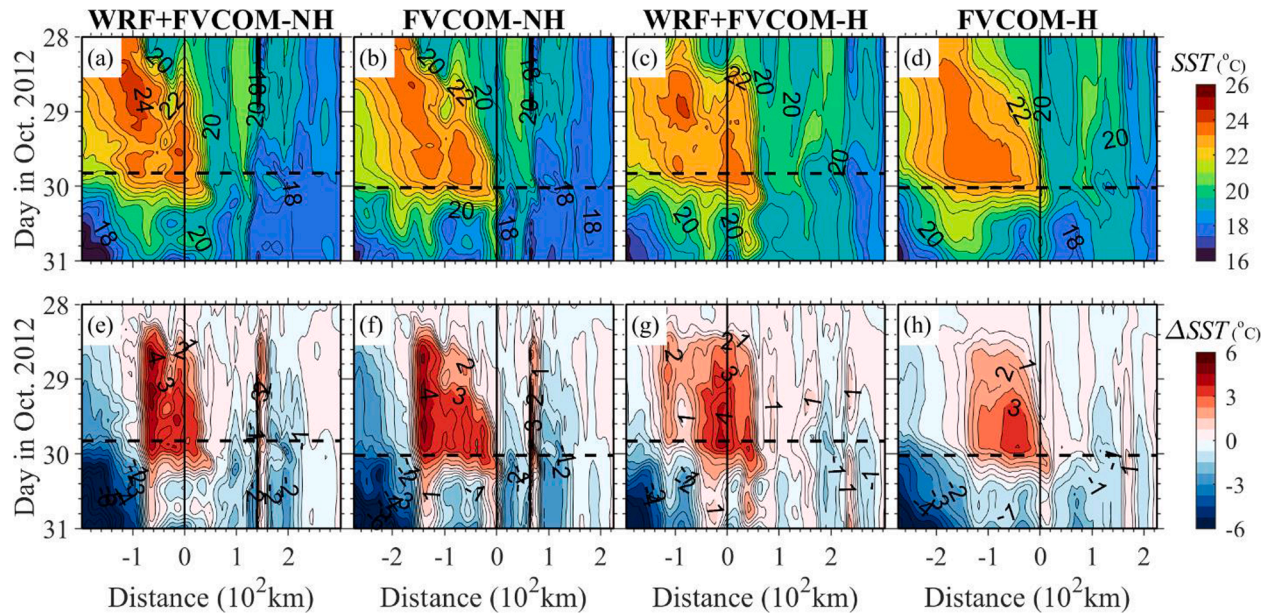


Fig. 20. The SST (a-d) and ΔSST (e-h) with time at S2 for the WRF + FVCOM-NH, FVCOM-NH, WRF + FVCOM-H, and FVCOM-H cases. ΔSST is the SST difference relative to the initial SST at 00:00 on 28 Oct. 2012. The y-axis is the time, and the x-axis is the distance relative to the hurricane center. Positive (negative) x: right (left) of the storm center. Black dashed lines: the time at which hurricane arrived at the transects; black solid lines: the origin of the x-axis, defined as the location of the hurricane center when the maximum inertial response is reached.

change over the slope featured a complex spatially variation pattern. The near-inertial responses to the clockwise rotating wind on the right side were not apparently visible as that in the open ocean.

We also examined the inertial response of the near-surface vertical velocity to the hurricane translation wind for the coupled and uncoupled H and NH cases. The near-surface vertical velocities predicted by WRF + FVCOM-NH and FVCOM-NH were generally one to two times stronger than the vertical velocities predicted by WRF + FVCOM-H and FVCOM-H (Figs. 21 and 22). On both S1 and S2, the change of the simulated near-surface vertical velocity before and after the hurricane crossing was

more prominent on the right side, more evident in the WRF + FVCOM-NH and FVCOM-NH results than in the WRF + FVCOM-H and FVCOM-H results (Figs. 21 and 22).

On S1, the WRF + FVCOM-NH results showed a maximum SST increase in an area 100 km away from the hurricane center on the right (Fig. 19a, e). In this area, the near-surface vertical velocity experienced a considerable drop after the hurricane passed (Fig. 21a, e). Meanwhile, the WRF + FVCOM-NH also predicted a dramatic decrease in near-surface vertical velocity in an area about 50 km away from the hurricane center, where a substantial SST drop was found (Fig. 21a, e). It

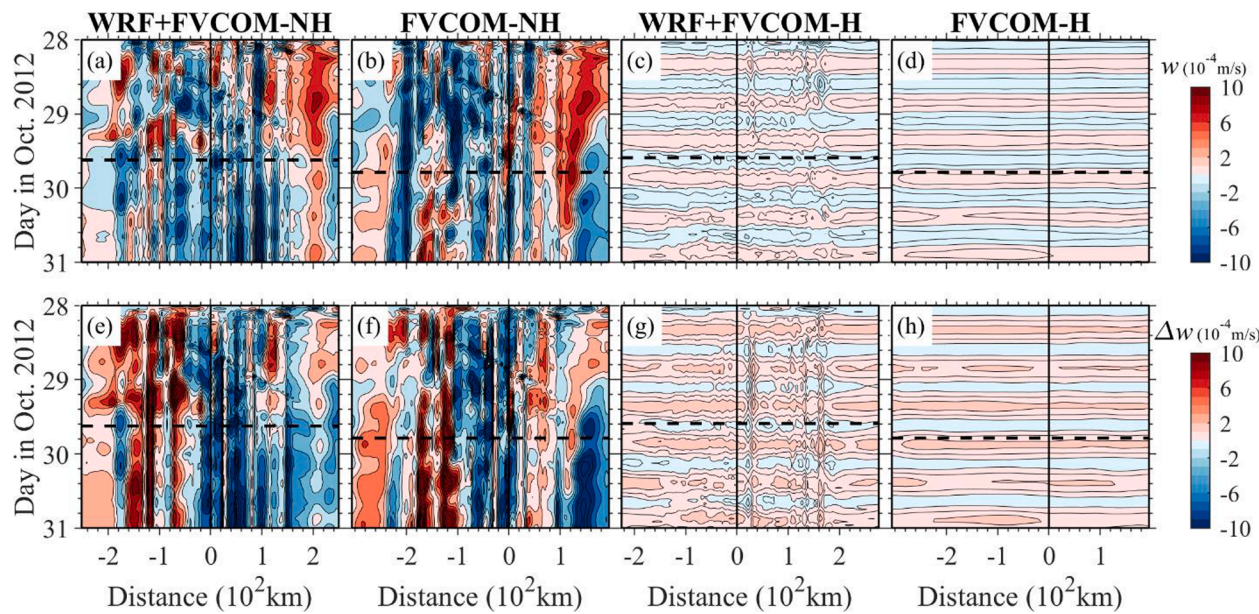


Fig. 21. The changes of the near-surface vertical velocity (w) (a-d) and Δw (e-h) with time at S1 for the WRF + FVCOM-NH, FVCOM-NH, WRF + FVCOM-H, and FVCOM-H cases. Δw is the w difference relative to the initial w at 00:00 on 28 Oct. 2012. The y-axis is the time, and the x-axis is the distance relative to the hurricane center. Positive (negative) x: right (left) of the storm center. Black dashed lines: the time at which hurricane arrived at the transects; black solid lines: the origin of the x-axis, defined as the location of the hurricane center when the maximum inertial response is reached.

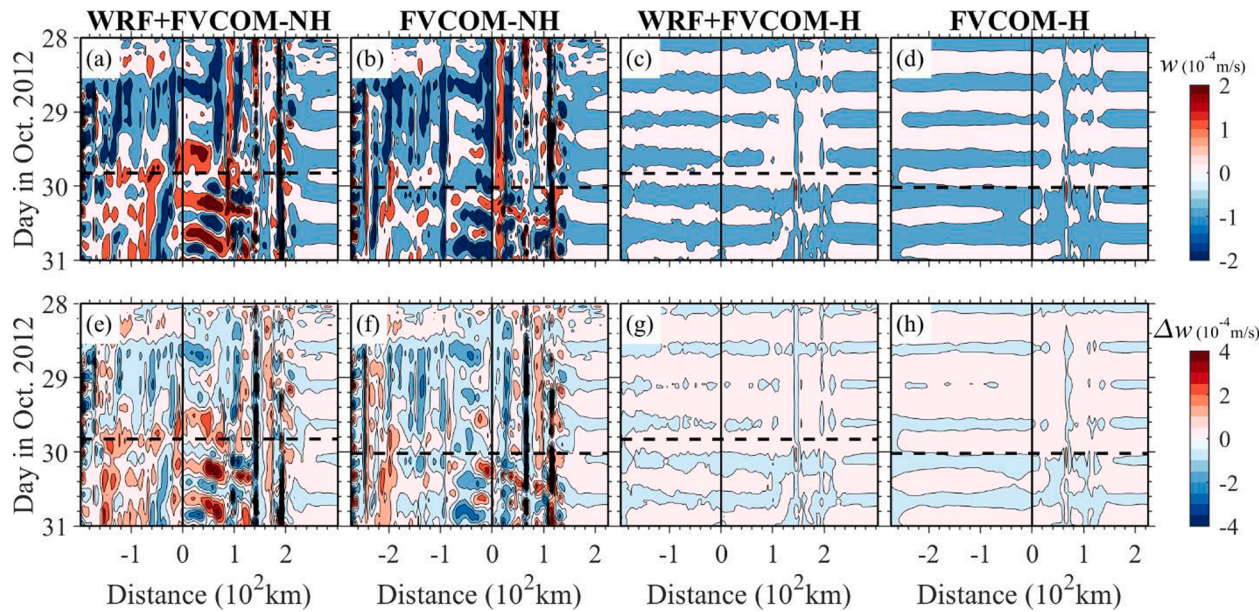


Fig. 22. The changes of the near-surface vertical velocity (w) (a-d) and Δw (e-h) with time at S2 for the WRF + FVCOM-NH, FVCOM-NH, WRF + FVCOM-H, and FVCOM-H cases. Δw is the w difference relative to the initial w at 00:00 on 28 Oct. 2012. The y-axis is the time, and the x-axis is the distance relative to the hurricane center. Positive (negative) x: right (left) of the storm center. Black dashed lines: the time at which hurricane arrived at the transects; black solid lines: the origin of the x-axis, defined as the location of the hurricane center when the maximum inertial response is reached.

implied that the SST drop in that area might be caused by other physical mechanisms. The WRF + FVCOM-H results showed a maximum SST increase in an area 120 km away from the hurricane center (Fig. 19c, f). The near-surface vertical velocity predicted in this case varied with the semidiurnal M_2 tidal period (Fig. 21c,g). Although the variation amplitude was slightly more substantial on the right side, no significant different amplitude variation was found around that area. The coupled NH model predicted a more substantial near-surface vertical velocity

than the uncoupled NH model. Their distributions on S1 were also different.

On S2, the changes in the near-surface vertical velocity before and after the hurricane crossing were also more substantial on the right side than on the left side (Fig. 22). The WRF + FVCOM-NH results showed a higher SST in a narrow area 150 km away from the hurricane center and large SST drops on both sides of that area after the hurricane passed (Fig. 20a, e). In these areas, the near-surface vertical velocity showed a

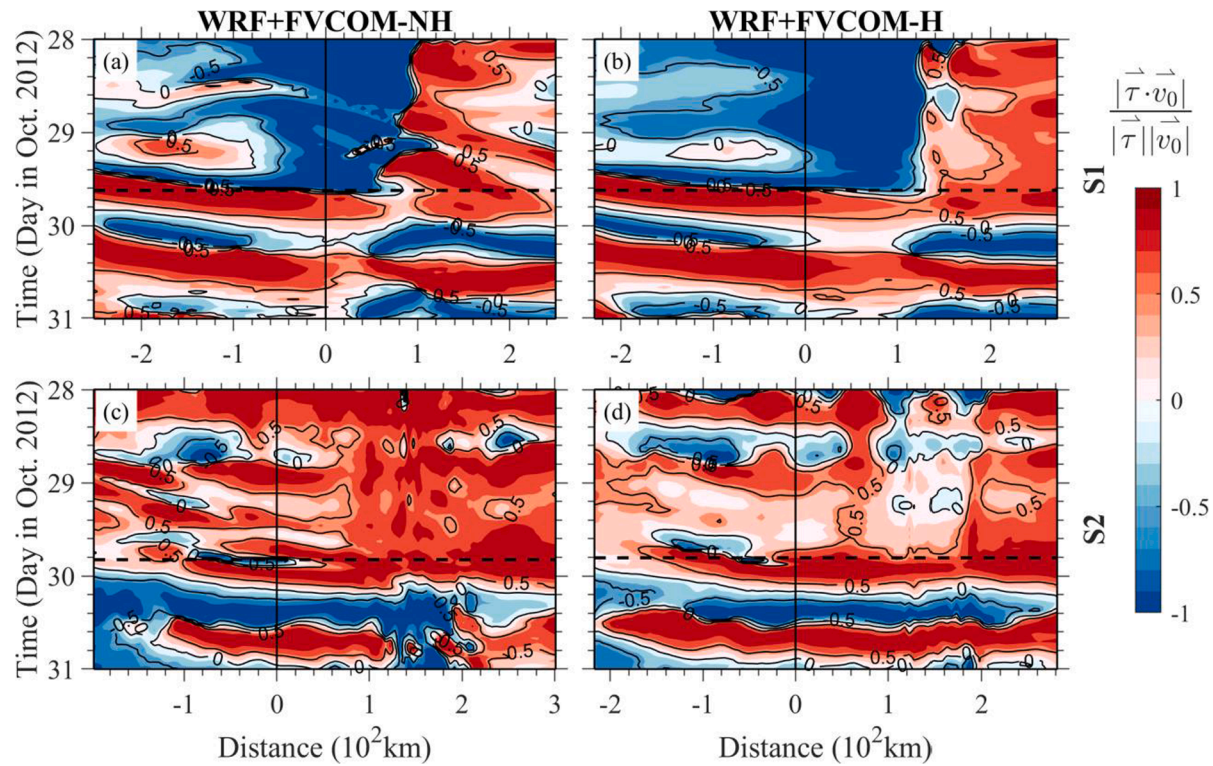


Fig. 23. The cosine angle between the wind stress and the oceanic surface velocity at S1 (a-b) and S2 (c-d) for the WRF + FVCOM-NH and WRF + FVCOM-H cases. Black dashed lines: the time of hurricane arriving the transects; black solid lines: the origin of the x-axis, defined as the location of the hurricane center when the maximum inertial response is reached. Positive (negative) x: right (left) of the storm center.

relatively strong temporospatial variation, but it was not robustly correlated to the SST changes in those areas (Fig. 22a, e). In the WRF + FVCOM-H case, the maximum changes in the near-surface vertical velocity were in the areas 150 and 200 km away from the hurricane center (Fig. 22c, g). The big SST drop around 200 km on the right side after the hurricane passed seemed to correlate well with a considerable increase of the near-surface vertical velocity when the hurricane arrived over there. However, the substantial variation in the near-surface vertical velocity around 150 km seemed not to correlate with the SST change in that area. Similar features were also found in the FVCOM-NH and FVCOM-H cases.

Price (1981) examined the efficiency of the oceanic response with the angle between the wind stress and the oceanic surface velocity. He found that the response occurs when the wind direction is in a positive phase with the current direction, with a maximum when they are in the same direction. The change of the wind-current angle with time was examined on S1 and S2 for the coupled cases (Fig. 23). On S1, the normalized positive angle increased dramatically when the hurricane arrived. The value was > 0.5 during the near-resonance period on 29 Oct. On S2, the cosine value during the near-resonance could reach 1.0. It indicated that on both S1 and S2, the wind-current angles were under a favorable condition to generate substantial oceanic responses. The non-hydrostatic case showed a higher efficiency of energy transferring from wind to the ocean at the air-sea interface on the right of the storm center.

5. Summary

We have examined the influence of the oceanic process on the intensity, path, and landfall of Hurricane Sandy and the impact of the air-sea interaction on the hurricane-induced variation of the oceanic currents, water elevation, temperature, and mixing over the U.S. northeastern shelf under the H and NH conditions.

For the hurricane simulation, the H and NH coupled WRF-FVCOMs

have consistently demonstrated that including oceanic processes in WRF can substantially improve the simulation of Sandy's intensity and tracks. When the hurricane moved towards the coast, the local OML rapidly deepened with increased storm winds. Intense vertical mixing brought cold water in the deep ocean towards the surface, producing a cold wake underneath the storm, with the lowest sea temperature at the maximum wind zone. This process led to a sizeable latent heat loss from the ocean within the storm and hence rapid drops of the air temperature and vapor mixing ratio above the sea surface. As a result, the storm intensified as the central sea-level air pressure dropped. Improving air pressure simulation with OML tended to reduce the storm size and strengthen the storm intensity and hence provided a better simulation of hurricane path and landfall. The coupled model-predicted distributions of the maximum latent heat flux loss on the left and rear area of the hurricane center were consistent with the OceanSat-2 satellite-derived surface wind distribution of Hurricane Sandy. The observed asymmetric wind field with a maximum on the left side resulted from a significant energy gain from the enhanced latent heat flux in the left and rear areas and a loss of the latent heat flux in the front and right places. Turning on the NH process slightly improved the hurricane central SLP simulation and intensified the winds.

For the ocean, both WRF + FVCOM-H and WRF + FVCOM-NH captured Sandy-induced rapidly-varying flow over the shelf and the wind-induced surge level at the coast. The coupled models predicted a higher water elevation around the coastal areas where Hurricane Sandy made landfall than the uncoupled model. The uncoupled and coupled models both showed more substantial oceanic responses on the right side of the hurricane center, with a maximum during the Sandy crossing period when the clockwise-rotating frequency of Sandy wind was close to the local inertial frequency. It was evident in the changes in SST and vertical velocity. The area with a maximum response varied with Sandy's translation speed, more prominent in the deep region than over the slope. The near-inertial resonance oceanic responses to tropical storms were first discovered by Price (1981), and our findings agreed well with

his theories.

WRF + FVCOM-H and WRF + FVCOM-NH predicted a substantially different temporospatial SST variation. The most considerable difference was on the right side of the hurricane center and over the slope, with a maximum SST difference was up to $\sim 2.0^{\circ}\text{C}$. The vertical velocity was about 2–3 times stronger in the WRF + FVCOM-NH simulation than in the WRF + FVCOM-H simulation, with substantial differences in the deep region during Sandy's crossing. Taking the hurricane center as a reference location, the WRF + FVCOM-NH predicted a deeper MLD on the right side and a shallower MLD on the left side, which matched the distribution of the vertical velocity difference between NH and H models. The maximum MLD difference could be up to ~ 20 m. The substantial vertical velocity difference found in the deep ocean off the slope suggests that the NH process-induced vertical velocity could enhance the SST change within the storm-influenced area, even though the model grid specified in the study could not fully resolve the NH convection.

It should be pointed out that based on the vertical to horizontal ratio, the WRF + FVCOM-NH experiments with a 2-km resolution grid did not fully resolve the non-hydrographic convection process in the continental shelf region. No substantial differences in water elevation and vertical velocity between WRF + FVCOM-NH and WRF + FVCOM-H were probably due to insufficient horizontal resolution specified in the NH case. A refined grid with numerical and physical consistency should be considered to re-examine the impacts of the non-hydrostatic process on the air-sea interaction over the continental shelf.

Our experiments did not examine the influence of wind-current-wave interactions on hurricane intensity, heat transfer, currents, and water elevation. [Zhang and Perrie \(2001\)](#) found that the change in surface ocean roughness due to waves could influence the wind intensity

and air-sea heat fluxes. The wind could be weakened in an area where wind waves are energetic, enhancing wind asymmetry. [Olabarrieta et al. \(2012\)](#) applied COWAST to simulate Hurricane Ida. They observed similar features as those reported in [Zhang and Perrie \(2001\)](#). Meanwhile, their results showed that waves impact is more significant in the nearshore region, which tended to cause the cyclone to deviate eastwards before the landfall. We have implemented three wave-related surface roughness parameterization equations in WRF-FVCOM. This paper compared hydrostatic and nonhydrostatic processes in the coupled model. A further investigation of the wave's impacts should be taken into consideration.

Declaration of Competing Interest

The authors declare that they have no known competing financial interests or personal relationships that could have appeared to influence the work reported in this paper.

Data availability

Data will be made available on request.

Acknowledgments

This research was supported by the NOAA-funded IOOS NERACOOS program for NECOFS with subcontract numbers A005, A008, and the NSF LTER project subcontracted from Woods Hole Oceanographic Institution. The authors would like to thank Drs. Kenneth H. Brink, Robert C. Beardsley, Wendell Brown, and Geoffrey W. Cowles for their valuable comments and suggestions.

Appendix A.: Time steps for the non-hydrographic model

The time step of the hydrostatic ocean model was decided based on the CFL criterion by considering the horizontal resolution and topographic slope. However, the time step for the non-hydrostatic model requires considering not only the numerical stability but also numerical convergence under a given model grid. We found that the numerical solution over the steep bottom slope varied with the integration time step for the given horizontal and vertical grids. These variations are due to the numerical errors of topographic coordinates. A set of experiments were done to determine the proper time step to minimize the topographic coordinate-induced numerical error over the steep slope with FVCOM-NH. For a given 2-km refined grid, the FVCOM-NH was tested with the time step of 10.0, 5.0, and 2.0 s. In all these cases, the model was integrated for 10 days, starting from 00:00 on 18 Oct. 2012 to 00:00 on 28 Oct. 2012, before the hurricane entered the ocean model domain.

The 10-day simulation results showed that the FVCOM-NH could remain numerically stable with large time steps, but the numerical solution over the steep slope varied with the time step, especially in the vertical velocity. The vertical velocity reduced as the time step became small ([Fig. A1](#)). The numerical solution remained the same when the time step was 2 s or less. We believe the 2 s time step is proper to control the topographic coordinate errors. Based on these test results, we selected 2 s as the time step for FVCOM-NH experiments.

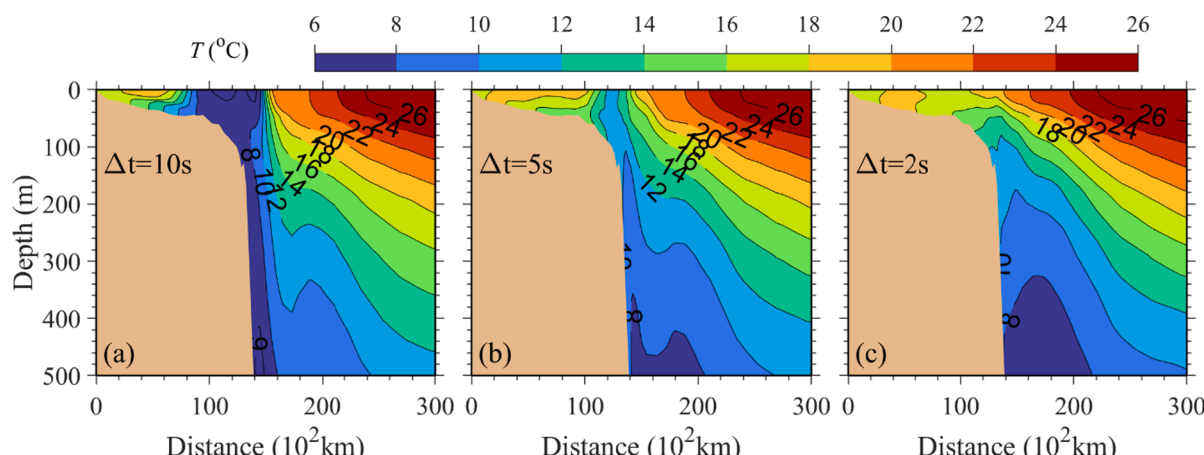


Fig. A1. The cross-shelf distributions of the temperature predicted by FVCOM-NH with time steps of 10 (a), 5 (b), and 2 (c) s.

Appendix B: Determination of inertial resonance radius

Eq. (1) in the text was derived from four assumptions. Assumption 1 was that the storm moved towards the coast at a constant speed, with a turning angle radius larger than the distance from the storm center to the location of the maximum response. It could avoid a sharply turning case that is unsolvable analytically. Assumption 2 was that the maximum response could occur anywhere on the right side as long as the wind rotating reached a near-inertial frequency, so we could only consider a situation with a 90° to the right. Assumption 3 was that the superposition effect of translation speed on the cyclonic rotary wind was negligible so that the rotating frequency of the wind at a site could be directly determined by the model-simulated wind at that location. Assumption 4 was that it was an idealized storm in which the friction-induced cross-air pressure isogeostrophic flow was neglected.

Suppose that a storm moves northward at a translation speed of U_H , successively across locations of P_1 , P_2 , and P_3 (Fig. B1a). A fixed point O is selected on the right side. When the storm center is at P_2 , the distance from O to the storm center reaches its minimum, with the length of R . From P_1 to P_2 and P_2 to P_3 , the storm center rotates an angle of θ relative to O . When only the storm tangential wind is considered, the wind direction (W_1 , W_2 , and W_3) at O rotated a radian of θ , correspondingly. The distance (l) and time (Δt) from P_1 to P_3 is.

$$l = 2R \tan \theta \quad (B.1)$$

$$\Delta t = \frac{2R \tan \theta}{U_H} \quad (B.2)$$

The wind rotating frequency (f_w) is.

$$f_w = \frac{2\theta}{\Delta t} \quad (B.3)$$

Based on Price (1981)'s results, the resonant response occurs when the wind on the right side rotates with the local inertial period, i.e., f_w is close to the Coriolis frequency (f). When the ocean response reaches the maximum, the relation between U_H and R is derived as:

$$\frac{U_H}{R} = \frac{f}{\theta} \tan \theta \quad (B.4)$$

The radius of the position with maximum oceanic response to a storm is proportional to the translation speed at a given latitude.

For a more general situation, when a storm turns right or left, the location of the maximum oceanic response varies (Fig. B1b, c). Suppose a storm

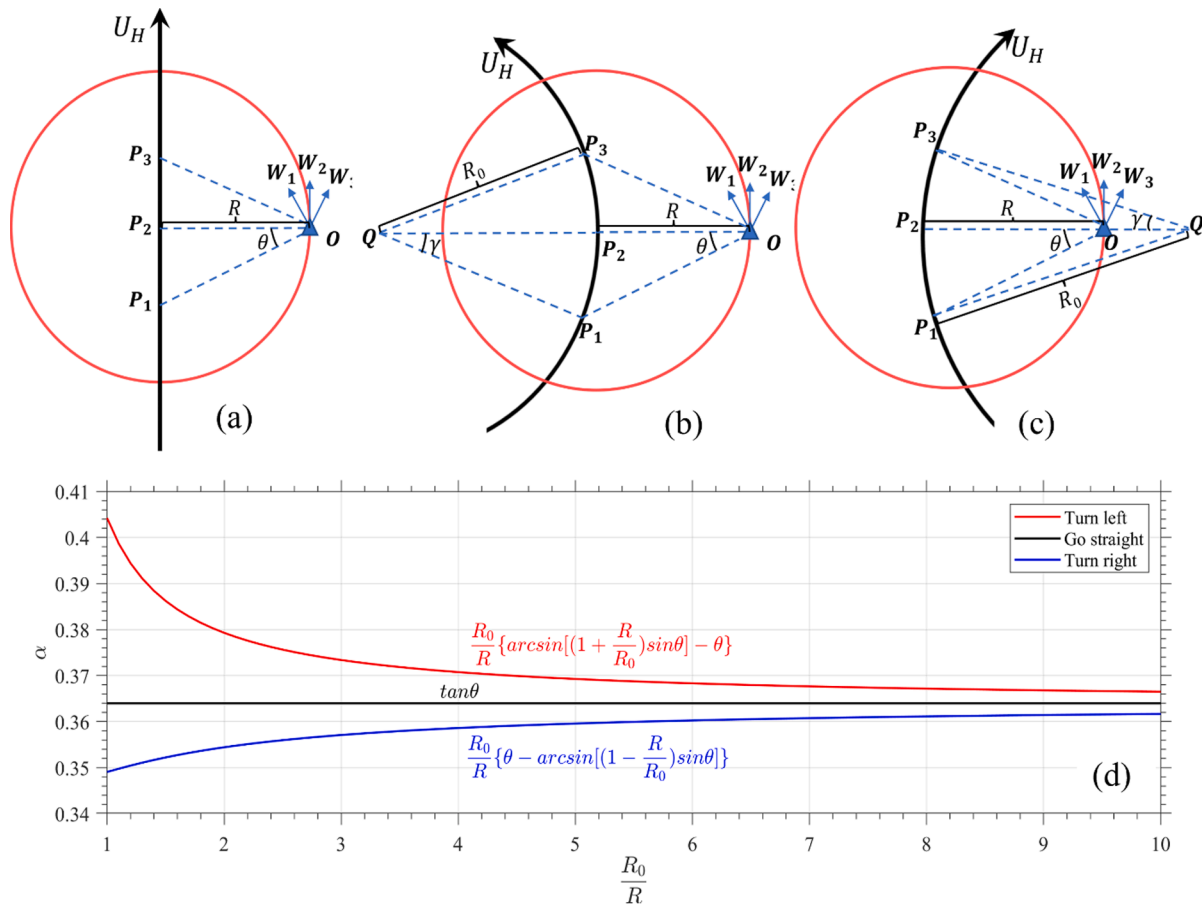


Fig. B1. The sketch of wind rotation at a fixed position on the right side of a storm in the situations of going straight (a), turning left (b), and turning right (c), and the change of α with $\frac{R_0}{R}$ (d). In (a-c), red circle: the radius of R relative to the storm center; blue triangle: the fixed position on the right side of the storm center; black arrow: the storm translation direction.

moves in a circle centered at Point Q with a curvature of R_0 . If its track does not turn sharply ($R_0 > R$), Eq. (B.2) can be rewritten as.

$$\Delta t = \frac{2R_0 \tan \gamma}{U_H} \quad (B.5)$$

where γ is the half radian of the track turns around Q. According to the Law of Sines:

$$\frac{R_0 + R}{\sin(\pi - \gamma - \theta)} = \frac{R_0}{\sin \theta}, \text{ as the storm turned left} \quad (B.6)$$

$$\frac{R_0 - R}{\sin(\theta - \gamma)} = \frac{R_0}{\sin(\pi - \theta)}, \text{ as a storm turned right} \quad (B.7)$$

According to Eqs. B.3–7, the relation between U_H and R can be derived as:

$$\frac{U_H}{R} = \frac{f}{\theta} \alpha \quad (B.8)$$

where

$$\alpha = \begin{cases} \frac{R_0}{R} \left\{ \arcsin \left[\left(1 + \frac{R}{R_0} \right) \sin \theta \right] - \theta \right\}, & \text{turning left} \\ \tan \theta, & \text{go straight} \\ \frac{R_0}{R} \left\{ \theta - \arcsin \left[\left(1 - \frac{R}{R_0} \right) \sin \theta \right] \right\}, & \text{turning right} \end{cases} \quad (B.9)$$

For a given latitude, R is proportional to U_H , i.e.,

$$R = \gamma U_H \quad (B.10)$$

where $\gamma = \frac{\theta}{f \alpha}$. Compared with the situation of moving straight, the adjustment of R due to the storm translation curvature is minor (Fig. B.1d). When R_0 is twice larger than R , R decreases by 4.2% when a storm turns left and increases by 2.6% when moving left.

References

Anthes, R.A., 1974. The dynamics and energetics of mature tropical cyclones. *Rev. Geophys. Space Phys.* 21 (3), 495–522.

Beardsley, R.C., Chen, C., Xu, Q., 2013. Coastal flooding in Scituate (MA): a FVCOM study of the 27 December 2010 nor'easter. *J. Geophys. Res. Oceans* 118, 6030–6045.

Beji, S., Nadaoka, K., 1994. Numerical simulation of nonlinear directional waves by an improved Boussinesq model. *Waves-Physical and Numerical Modeling*, Vancouver, Canada 1, 534–543.

Bernier, N.B., Thompson, K.R., 2006. Predicting the frequency of storm surges and extreme sea levels in the northwest Atlantic. *J. Geophys. Res.* 111, C10009.

Blake, E. S., T. B. Kimberlain, R. J. Berg, J. P. Cangialosi and J. L. Beven II (2013), Tropical Cyclone Report: Hurricane Sandy (AL182012) October 22–29, 2012. *National Hurricane Center*, 157pp.

Burchard, H., 2002. *Applied turbulence modelling in marine waters*, Vol. 100. Springer Science and Business Media.

Charney, J.G., Eliassen, A., 1964. On the growth of the hurricane depression. *J. Atmos. Sci.* 21, 68–75.

Chen, C., Qin, Z., 1985a. Numerical simulation of typhoon surges along the east coast of Zhejiang and Jiangsu Provinces. *Advance in Atmospheric Sciences* 2 (11), 8–19.

Chen, C., Qin, Z., 1985b. Dynamic analysis of typhoon surges along the east coast of Zhejiang and Jiangsu Provinces. *Acta Oceanographic Sinica* 4 (4), 516–526.

Chen, C., Qin, Z., 1985c. On geostrophic adjustment process of oceanic motions. *Scientia Sinica, Series B* Vol. XXVIII No. 10, 1093–1100.

Chen, C., Beardsley, R.C., 1995. A numerical study of stratified tidal rectification over finite-amplitude banks. Part I: Symmetric banks. *J. Phys. Oceanogr.* 25 (9), 2090–2110.

Chen, C., Reid, R., Nowlin Jr., W.D., 1996. Near-inertial oscillations over the Texas-Louisiana shelf. *J. Phys. Oceanogr.* 101, 3509–3524.

Chen, C., Liu, H., Beardsley, R.C., 2003. An unstructured grid, finite-volume, three-dimensional primitive equations ocean model: application to coastal ocean and estuaries. *J. Atmos. Oceanic Technol.* 20, 159–186.

Chen, C., Beardsley, R.C., Hu, S., Xu, Q., Lin, H., 2005. Using MM5 to hindcast the ocean surface forcing fields over the Gulf of Maine and Georges Bank region. *J. Atmos. Oceanic Technol.* 22 (2), 131–145.

Chen, C., Beardsley, R.C., Cowles, G., 2006. An unstructured-grid, finite-volume coastal ocean model (FVCOM) system. *Oceanography* 19 (1), 78–89.

Chen, C., Qi, J., Li, C., Beardsley, R.C., Lin, H., Walker, R., Gates, K., 2008. Complexity of the flooding/drying process in an estuarine tidal-creek salt-marsh system: an application of FVCOM. *J. Geophys. Res. Oceans* 113, C07052.

Chen, C., Malanotte-Rizzoli, P., Wei, J., Beardsley, R.C., Lai, Z., Xue, P., Lyu, S., Xu, Q., Qi, J., Cowles, G.W., 2009. Application and comparison of Kalman filters for coastal ocean problems: an experiment with FVCOM. *J. Geophys. Res. Oceans* 114 (C5).

Chen, C., Beardsley, R.C., Cowles, G., Qi, J., Lai, Z., Gao, G., Stuebe, D., Xu, Q., Xue, P., Ge, J., Ji, R., Hu, S., Tian, R., Huang, H., Wu, L., Lin, H., 2013a. An unstructured-grid, finite-volume community ocean model: FVCOM user manual. Sea Grant College Program, Massachusetts Institute of Technology, Cambridge, MA, USA.

Chen, C., Beardsley, R.C., Luettich Jr., R.A., Westrink, J.J., Wang, H., Perrie, W., Xu, Q., Donahue, A.S., Qi, J., Lin, H., Zhao, L., Kerr, P.C., Meng, Y., Toulan, B., 2013b. Extratropical storm inundation testbed: Inter-model comparisons in Scituate Massachusetts. *J. Geophys. Res. Oceans* 118, 5054–5073.

Chen, C., Gao, G., Zhang, Y., Beardsley, R.C., Lai, Z., Qi, J., Lin, H., 2016. Circulation in the Arctic Ocean: results from a high-resolution coupled ice-sea nested Global-FVCOM and Arctic-FVCOM system. *Prog. Oceanogr.* 141, 60–80.

Chen, C., Lin, Z., Beardsley, R.C., Shyka, T., Zhang, Y., Xu, Q., Qi, J., Lin, H., Xu, D., 2021a. Impacts of sea-level rise on future storm-induced coastal inundations over Massachusetts coast. *Nat. Hazards* 106, 375–399.

Chen, C., Zhao, L., Gallager, S., Ji, R., He, P., Davis, C., Beardsley, R.C., Hart, D., Gentleman, W.C., Wang, L., Li, S., Lin, H., Stokebury, K., Bethoney, D., 2021b. Impact of larval behaviors on dispersal and connectivity of sea scallop larvae over the northeast U.S. shelf. *Prog. Oceanogr.* 195, 102604.

Chen, S.S., Zhao, W., Donelan, M.A., Tolman, H.L., 2013c. Directional wind-wave coupling in fully coupled atmosphere-wave-ocean models: results from CBLAST-Hurricane. *J. Atmos. Sci.* 70, 3198–3215.

Cione, J.J., Uhlhorn, E.W., 2003. Sea surface temperature variability in hurricanes: Implications with respect to intensity change. *Mon. Weather Rev.* 131 (8), 1783–1796.

Cowles, G.W., 2008. Parallelization of the FVCOM Coastal Ocean Model. *Int. J. High-Perform. Comput. Appl.* 22 (2), 177–193.

Dare, R.A., McBride, J.L., 2011. Sea surface temperature response to tropical cyclones. *Mon. Weather Rev.* 139, 3798–3808.

Darwish, M.S., Moukalled, F., 2003. TVD schemes for unstructured grids. *Int. J. Heat Mass Transf.* 46 (4), 599–611.

Davis, C.W., Wang, S.S., Chen, Y., Chen, K., Corbosiero, M., DeMaria, J., Dudhia, G., Holland, J., Klemp, J., Michalakes, H., Reeves, R., Rotunno, C.S., Xiao, Q., 2008. Prediction of landfalling hurricanes with the Advanced Hurricane WRF model. *Mon. Weather Rev.* 136, 1990–2005.

Dewar, W.K., Flierl, G.R., 1987. Some effects of the wind on rings. *J. Phys. Oceanogr.* 17 (10), 1653–1667.

Diakakis, M., Deligiannakis, G., Katsetsiadou, K., Lekkas, E., 2015. Hurricane Sandy mortality in the Caribbean and continental North America. *Disaster Prev. Manage.* 24, 132–148.

Dong, W., Feng, Y., Chen, C., Wu, Z., Xu, D., Li, S., Xu, Q., Wang, L., Beardsley, R.C., Lin, H., Li, R., Chen, J., Li, J., 2021. Observational and modeling studies of oceanic responses and feedbacks to Typhoons Hato and Mangkhut over the northern shelf of the South China Sea. *Prog. Oceanogr.* 191, 102507.

Drennan, W.M., Gruber, H.C., Hauser, D., Quentin, C., 2003. On the wave age dependence of wind stress over pure wind seas. *J. Geophys. Res. Oceans* 108, 8062.

Duhaup, T.H., Straub, D.N., 2006. Wind stress dependence on ocean surface velocity: Implications for mechanical energy input to ocean circulation. *J. Phys. Oceanogr.* 36 (2), 202–211.

Edson, J.B., Jampala, V., Weller, R.A., Bigorre, S.P., Plueddemann, A.J., Fairall, C.W., Miller, S.D., Mahrt, L., Vickers, D., Hersbach, H., 2013. On the exchange of momentum over the open ocean. *J. Phys. Oceanogr.* 43 (8), 1589–1610.

Emanuel, K.A., 2003. Tropical cyclones. *Annu. Rev. Earth Planet. Sci.* 31, 75–104.

Fairall, C.W., Bradley, E.F., Godfrey, J.S., Wick, G.A., Edson, J.B., Young, G.S., 1996. Cool-skin and warm-layer effects on sea surface temperature. *J. Geophys. Res. Oceans* 101, 1295–1308.

Frank, W.M., 1987. Tropical cyclone formation (Chapter 3). In: Elsberry, R.L. (Ed.), *Global view of tropical cyclones*. Office of Naval Research, pp. 53–90.

Gao, G., Chen, C., Qi, J., Beardsley, R.C., 2011. An unstructured grid, finite-volume sea ice model: Development, validation, and application. *J. Geophys. Res. Oceans* 116, C00D04.

Ge, J., Chen, C., Wang, Z., Ke, K., Yi, J., Ding, P., 2020. Dynamic response of the fluid mud to a tropical storm. *J. Geophys. Res. Oceans* 125 (3).

Glenn, S. M., T. N. Miles, G. N. Seroka, Y. Xu, R. K. Forney, F. Yu, H. Roarty, O. Schofield and J. Kohut (2016), Stratified coastal ocean interactions with tropical cyclones. *Nature Communications*, 7 (10887).

Gochis, D.J., Barlage, M., Cabell, R., Casali, M., Dugger, A., FitzGerald, K., McAllister, M., McCreight, J., RafieeiNasab, A., Read, L., Sampson, K., Yates, D., Zhang, Y., 2020. The WRF-Hydro modeling system technical description (Version 5.1.1). NCAR Technical Note, 107, pages.

Greenspan, H.P., 1968. The theory of rotating fluids. Cambridge University Press, p. 327.

Grell, G.A., Peckham, S.E., Schmitz, R., McKeen, S.A., Frost, G., Skamarock, W.C., Eder, B.B., 2005. Fully coupled “online” chemistry within the WRF model. *Atmos. Environ.* 39 (37), 6957–6975.

Hill, C., DeLuca, C., Suarez, M., DA Silva, A., 2004. The architecture of the earth system modeling framework. *Comput. Sci. Eng.* 6, 18–28.

Janjić, Z.I., 1994. The step-mountain eta coordinate model: further developments of the convection, viscous sublayer, and turbulence closure schemes. *Mon. Weather Rev.* 122, 927–945.

Jeworrek, J., West, G., Stull, R., 2019. Evaluation of cumulus and microphysics parameterizations in WRF across the convective gray zone. *Weather Forecasting* 34 (4), 1097–1115.

Jones, H., Marshall, J., 1993. Convection with rotation in a neutral ocean: a study of open-ocean deep convection. *J. Phys. Oceanogr.* 23 (6), 1009–1039.

Kang, X., Xia, M., 2020. The study of the hurricane-induced storm surge and bay-ocean exchange using a nesting model. *Estuaries Coasts* 43, 1610–1624.

Knapp, K.R., Kruk, M.C., Levinson, D.H., Diamond, H.J., Neumann, C.J., 2010. The International Best Track Archive for Climate Stewardship (IBTrACS): unifying tropical cyclone best track data. *Bull. Am. Meteorol. Soc.* 91, 363–376.

Kobayashi, M.H., Pereira, J.M., Pereira, J.C., 1999. A conservative finite-volume second-order-accurate projection method on hybrid unstructured grids. *J. Comput. Phys.* 150 (1), 40–75.

Kundu, P.K., 1986. A two-dimensional model of inertial oscillations generated by a propagating wind field. *J. Phys. Oceanogr.* 16, 1076–1084.

Lai, Z., Chen, C., Cowles, G.W., Beardsley, R.C., 2010a. A non-hydrostatic version of FVCOM, Part I: validation experiments. *J. Geophys. Res. Atmos.* 115, C11010.

Lai, Z., Chen, C., Cowles, G.W., Beardsley, R.C., 2010b. A nonhydrostatic version of FVCOM, Part II: mechanistic study of tidally generated nonlinear internal waves in Massachusetts Bay. *J. Geophys. Res.* 115, C12049.

Lai, Z., Jin, G., Huang, Y., Chen, H., Shang, X., Xiong, X., 2019. The generation of nonlinear internal waves in the South China Sea: a three-dimensional, nonhydrostatic numerical study. *J. Geophys. Res. Oceans* 124 (12), 8949–8968.

Large, W.G., Pond, S., 1981. Open-ocean momentum flux measurements in moderate to strong winds. *J. Phys. Oceanogr.* 11, 324–336.

Lee, C.-Y., Chen, S.S., 2014. Stable boundary layer and its impact on tropical cyclone structure in a coupled atmosphere-ocean model. *Mon. Weather Rev.* 142, 1927–1944.

Li, S., Chen, C., Wu, Z., Beardsley, R.C., Li, M., 2020. Impacts of oceanic mixed layer on hurricanes: a simulation experiment with Hurricane Sandy. *J. Geophys. Res. Oceans* 125 e2019JC015851.

Li, R., Chen, C., Dong, W., Beardsley, R.C., Wu, Z., Gong, W., 2021. Slope-intensified storm-induced near-inertial oscillations in the South China Sea. *J. Geophys. Res. Oceans* 126 e2020JC016713.

Lin, I.-I., Liu, W.T., Wu, C., Wong, G.T.F., Hu, C., Chen, Z., Liang, W., Yang, Y., Liu, K., 2003. New evidence for enhanced ocean primary production triggered by tropical cyclone. *Geophys. Res. Lett.* 30 (13).

Lin, I.-I., Wu, C.-C., Emanuel, K.A., Lee, I.H., Wu, C.R., Pun, I.F., 2005. The interaction of super typhoon Maemi (2003) with a warm ocean eddy. *Mon. Weather Rev.* 133, 2635–2649.

Lin, I.-I., Wu, C., Pun, I., 2008. Upper-ocean thermal structure and the Western North Pacific Category 5 typhoons. Part I: ocean features and the Category 5 typhoons’ intensification. *Mon. Weather Rev.* 136, 3288–3306.

Lin, I.-I., Pun, I.-F., Wu, C.-C., 2009. Upper-ocean thermal structure and the western North Pacific category-5 typhoons-Part II: Dependence on translation speed. *Mon. Weather Rev.* 137, 3744–3757.

Lin, I.-I., Black, P., Price, J.F., Yang, C.-Y., Chen, S.S., Lien, C.-C., Harr, P., Chi, N.-H., Wu, C.-C., D’Asaro, E.A., 2013. An ocean coupling potential intensity index for tropical cyclones. *Geophys. Res. Lett.* 40, 1878–1882.

Marshall, J.C., Hill, L.P., Adcroft, A., 1997. Hydrostatic, quasi-hydrostatic and nonhydrostatic ocean modeling. *J. Geophys. Res.* 102 (C3), 5733–5752.

Mellor, G.L., Yamada, T., 1982. Development of a turbulence closure model for geophysical fluid problems. *Rev. Geophys.* 20 (4), 851–875.

Mooney, P.A., Gill, D.O., Mulligan, F.J., Bruyère, C.L., 2016. Hurricane simulation using different representations of atmosphere-ocean interaction: the case of Irene (2011). *Atmos. Sci. Lett.* 17 (7), 415–421.

Nuijens, L., Stevens, B., Siebesma, A.P., 2009. The environment of precipitating shallow cumulus convection. *J. Atmos. Sci.* 66 (7), 1962–1979.

Olabarrieta, M., Warner, J.C., Armstrong, B., Zambon, J.B., He, R., 2012. Ocean-atmosphere dynamics during Hurricane Ida and Nor’Ida: An application of the coupled ocean-atmosphere-wave-sediment transport (COAWST) modeling system. *Ocean Model.* 43, 112–137.

Oost, W.A., Komen, G.J., Jacobs, C.M.J., Oort, C.V., 2002. New evidence for a relation between wind stress and wave age from measurements during ASGAMAGE. *Bound.-Layer Meteorol.* 103 (3), 409–438.

Park, S.H., Skamarock, W.C., Klemp, J.B., Fowler, L.D., Duda, M.G., 2013. Evaluation of global atmospheric solvers using extensions of the Jablonowski and Williamson baroclinic wave test case. *Mon. Weather Rev.* 141, 3116–3129.

Pedlosky, J., 1986. Geophysical fluid dynamics, Second edition. Springer-Verlag, New York, p. 710.

Pollard, R.T., Rhines, P.B., Thompson, R.O., 1972. The deepening of the wind-mixed layer. *Geophys. Astrophys. Fluid Dyn.* 3, 381–404.

Powers, J.G., Stoelinga, M.T., 1999. A coupled air-sea mesoscale model: experiments in atmospheric sensitivity to marine roughness. *Mon. Weather Rev.* 128, 208–228.

Price, J.F., 1981. Upper-ocean response to a hurricane. *J. Phys. Oceanogr.* 11 (2), 153–175.

Price, J.F., 1983. Internal wave wake of a moving storm. Part I: scales, energy budget and observations. *J. Phys. Oceanogr.* 13 (6), 949–965.

Price, J.F., Weller, R.A., Pinkel, R., 1986. Diurnal cycling: Observations and models of the upper ocean response to diurnal heating, cooling, and wind mixing. *J. Geophys. Res. Oceans* 91 (C7), 8411–8427.

Price, J.F., Sanford, T.B., Forristall, G.Z., 1994. Forced stage response to a moving hurricane. *J. Phys. Oceanogr.* 24 (2), 233–260.

Price, J.F., 2009. Metrics of hurricane-ocean interaction: Vertically-integrated or vertically-averaged ocean temperature? *Ocean Sci.* 5, 351–368.

Qi, J., Chen, C., Beardsley, R.C., Perrie, W., Cowles, G.W., Lai, Z., 2009. An unstructured-grid finite-volume surface wave model (FVCOM-SWAVE): implementation, validations, and applications. *Ocean Model.* 28, 153–166.

Qi, J., Chen, C., Beardsley, R.C., 2018. FVCOM one-way and two-way nesting using ESMF: development and validation. *Ocean Model.* 124, 94–110.

Rego, J.L., Li, C., 2009. On the importance of the forward speed of hurricanes in storm surge forecasting: a numerical study. *Geophys. Res. Lett.* 36, L07609.

Roarty, H., Glenn, S., Brodie, J., Nazzaro, L., Smith, M., Handel, E., Kohut, J., Updyke, T., Atkinson, L., Boicourt, W., Brown, W., Seim, H., Muglia, M., Wang, H., Gong, D., 2020. Annual and seasonal surface circulation over the Mid-Atlantic Bight continental shelf derived from a decade of high-frequency radar observations. *J. Geophys. Res. Oceans* 125 e2020JC016368.

Schade, L.R., Emanuel, K.A., 1999. The ocean effect on the intensity of tropical cyclones: Results from a simple coupled atmosphere-ocean model. *J. Atmos. Sci.* 56 (4), 642–651.

Schlichting, H. (1979), Boundary-layer theory, translated by J. Kestin, Seventh edition. McGraw-Hill Book Company.

Seo, H. A. J. Miller and J. O. Roads (2007), The Scripps Coupled Ocean-Atmosphere Regional (SCOAR) Model, with applications in the Eastern Pacific Sector. *Journal of Climate*, 20, 381–402.

Skamarock, W. C., J. B. Klemp, J. Dudhia, D. O. Gill, D. Barker, M. G. Duda and J. G. Powers (2008), A description of the Advanced Research WRF version 3 (No. NCAR/ TN-475+STR). University Corporation for Atmospheric Research.

Smagorinsky, J., 1963. General circulation experiments with the primitive equations: I. the basic experiment. *Mon. Weather Rev.* 91 (3), 99–164.

Sun, L., Liang, X.-Z., Xia, M., 2020. Developing the coupled CWRF-FVCOM modeling system to understand and predict atmosphere-watershed interactions over the great lakes region. *J. Adv. Model. Earth Syst.* 12 e2020MS002319.

Sun, R., Subramanian, A.C., Miller, A.J., Mazloff, M.R., Hoteit, I., Cornuelle, B.D., 2019. SKRIPS v1. 0: a regional coupled ocean-atmosphere modeling framework (MITgcm-WRF) using ESMF/NUOPC, description and preliminary results for the Red Sea. *Geosci. Model Dev.* 12, 4221–4244.

Sun, Y., Chen, C., Beardsley, R.C., Ullman, D., Butman, B., Lin, H., 2016. Surface circulation in Block Island Sound and adjacent coastal and shelf regions: A FVCOM-CODAR comparison. *Prog. Oceanogr.* 143 (26–45), 20.

Taylor, P.K., Yelland, M.J., 2001. The dependence of sea surface roughness on the height and steepness of the waves. *J. Phys. Oceanogr.* 31 (2), 572–590.

Tian, R., Chen, C., Qi, J., Ji, R., Beardsley, R.C., Davis, C., 2015. Model study of nutrient and phytoplankton dynamics in the Gulf of Maine: patterns and drivers for seasonal and interannual variability. *ICES J. Mar. Sci.* 72 (2), 388–402.

Tiedtke, M., 1989. A comprehensive mass flux scheme for cumulus parameterization in large-scale models. *Mon. Weather Rev.* 117 (8), 1779–1800.

Wang, Z.-Q., Duan, A.-M., 2012. A new ocean mixed-layer model coupled into WRF. *Atmos. Oceanic Sci. Lett.* 5 (3), 170–175.

Warner, J.C., Armstrong, B., He, R., Zambon, J.B., 2010. Development of a coupled ocean-atmosphere-wave-sediment transport (COAWST) modeling system. *Ocean Model.* 35 (3), 230–244.

Weisberg, R. H. and L., Zheng (2006a), A simulation of the Hurricane Charley storm surge and its breach of North Captiva Island. *Florida Scientist*, 152–165.

Weisberg, R.H., Zheng, L., 2006b. Hurricane storm surge simulations for Tampa Bay. *Estuaries Coasts* 29, 899–913.

Weisberg, R.H., Zheng, L., 2008. Hurricane storm surge simulations comparing three-dimensional with two-dimensional formulations based on an Ivan-like storm over the Tampa Bay, Florida region. *J. Geophys. Res.* 113, C12001.

Wilhelmsson, R., J. Alameda, K. Droege, M. Folk, R. Fowler, D. Gannon, S. Graves, D. Haidvogel, P. Husbands, C. L. Isbell, D. Weber, P. Woodward, B. W. York, S. Anderson, B. Jewett, C. Moore, D. Nolan, D. Porter, D. Semeraro and S. Tanner (2004), MEAD (a Modeling Environment for Atmospheric Discovery). *20th International Conference on Interactive Information and Processing Systems (IIPS) for Meteorology, Oceanography and Hydrology*, 6.2.

Wu, C.-C., Lee, C.-Y., Lin, I.-I., 2007. The effect of the ocean eddy on tropical cyclone intensity. *J. Atmos. Sci.* 64, 3562–3578.

Wu, C.-C., Tu, W.-T., Pun, I.-F., Lin, I.-I., Peng, M.S., 2016. Tropical cyclone-ocean interaction in Typhoon Megi (2010)-a synergy study based on ITOP observations and atmosphere-ocean coupled model simulations. *J. Geophys. Res. Atmospheres* 121, 153–167.

Yablonsky, R.M., Ginis, I., Thomas, B., 2015. Ocean modeling with flexible initialization for improved coupled tropical cyclone-ocean model prediction. *Environ. Modell. Software* 67, 26–30.

Zeng, X., Beljaars, A., 2005. A prognostic scheme of sea surface skin temperature for modeling and data assimilation. *Geophys. Res. Lett.* 32 (14), L14605.

Zhang, Y., Chen, C., Beardsley, R.C., Gao, G., Qi, J., Lin, H., 2016. Seasonal and interannual variability of the Arctic Sea ice: a comparison between AO-FVCOM and observations. *J. Geophys. Res. Oceans* 121 (11).

Zhang, Y., Perrie, W., 2001. Feedback mechanism for the atmosphere and ocean surface. *Bound.-Layer Meteorol.* 100 (2), 321–348.